Exploring the efficiency of nitrogenated carbon quantum dots/TiO_2 S-scheme heterojunction in photodegradation ciprofloxacin in aqueous environments

Yılmaz ATEŞ[a], Zafer EROĞLU[b], Özkan AÇIŞLI[a], Önder METIN[b,c], Semra KARACA[a,*]

[a]Department of Chemistry, Faculty of Science, Atatürk University, 25240 Erzurum, Turkey

[b]Department of Chemistry, College of Sciences, Koç University, 34450 Sarıyer, Istanbul, Turkey

[c] Koç University Surface Science and Technology Center (KUYTAM), 34450 Sarıyer, Istanbul, Turkey

*Correspondence: skaraca@atauni.edu.tr

ORCIDs:

Yılmaz Ateş: https://orcid.org/0000-0003-0965-6279

Zafer Eroğlu: https://orcid.org/0000-0002-0601-2526

Özkan Açışlı: https://orcid.org/0000-0002-4465-0916

Önder Metin: https://orcid.org/0000-0003-1622-4992

Semra Karaca: https://orcid.org/0000-0001-8627-5803

Abstract: In this study, we developed a heterojunction photocatalyst, namely nitrogen-doped carbon quantum dots/titanium dioxide (*N*-CQDs/TiO_2), for the effective and sustainable treatment of ciprofloxacin (CIP) antibiotic from wastewater. Firstly, *N*-CQDs were prepared from chitosan biopolymer with a green, facile and effective hydrothermal carbonization technique and then it was anchored on the TiO_2 surface via a hydrothermal process. The morphological, structural, and optical properties of as-prepared materials were characterized by using advanced analytical techniques. The impacts of the mass percentage of *N*-CQDs, catalyst and CIP concentration, and pH on the photocatalytic CIP degradation were investigated in depth. Comparative analyses were performed to evaluate different processes including adsorption, photolysis, and photocatalysis for the removal of CIP with TiO_2 and *N*-CQDs/TiO_2. The results revealed that *N*-CQDs/TiO_2 exhibited the highest CIP removal efficiency up to 83.91% within 120 min using UVA irradiation under optimized conditions (10 mg/L CIP, 0.4 g/L catalyst, and pH 5). Moreover, the carbon source used in the fabrication of *N*-CQDs was also discussed, and the lower removal efficiency was obtained when glucose was used as a carbon source instead of chitosan. This perfect improvement in CIP degradation was imputed to the ideal separation and migration of photo-generated carriers, strong redox capability, and the high generation of reactive oxygen species (ROS) provided by the successful construction of *N*-CQDs/TiO_2 S-scheme heterojunction. Capturing experiments indicated that h^+ and •OH reactive oxygen species are the predominant factors for CIP elimination in water. Overall, this research presents a green synthesis approach for *N*-CQDs/TiO_2 heterojunction photocatalysts using natural materials, demonstrating its potential as a cost-effective and efficient method for pharmaceutical degradation in water treatment applications.

Keywords: Nitrogen-doped Carbon quantum dots, green synthesis, TiO_2, S-scheme heterojunction, photocatalyst, Ciprofloxacin degradation.

1. Introduction

The intensive use of pharmaceutical compounds such as various antibiotics and anti-inflammatories, and the resulting increase in their release into the receiving environment, has led to the emergence of a series of problems in the environment, particularly in water [1–3]. Ciprofloxacin (CIP), a fluoroquinolone antibiotic derivative, has a wide range of utilization in the treatment of humans and animals, and even in low concentrations, residues of CIP antibiotics can provoke serious problems that threaten human health and aquatic ecosystems [3,4]. Because of the high bacterial resistance and lower biodegradability of sewages containing CIP, its removal from wastewater is of great importance in concerning human health [3]. In this regard, to remove CIP and its metabolites in water, advanced oxidation processes (AOPs) such as sonocatalytic, photocatalytic, and Fenton have received much attention [3-5]. Semiconductor-based photocatalytic processes, recognized as environmentally friendly solutions, represent a promising avenue for addressing water treatment challenges. It is anticipated that these methods, employing high-performance and eco-friendly catalysts, could serve as optimal solutions in the quest for efficient water treatment [6]. To achieve high photocatalytic performance in the presence of a semiconductor photocatalyst, variables such as sunlight harvesting ability, high charge separation and transfer, and the occurrence of active sites for the photoredox reactions are critical. Moreover, the preparation of such an effective photocatalyst from natural resources using simple and inexpensive methods is important for a sustainable environment[7]. Therefore, the synthesized catalyst has a high pay in the success of photocatalytic processes. TiO_2 has been the most preferred semiconductor due to its low environmental toxicity, wonderful oxidation features, high chemical stability and inexpensiveness [8]. Since the bandgap of TiO_2 is 3.2 to 3.5 eV, the production of photo-generated carriers responsible for its photocatalytic properties requires exposure to ultraviolet light [8, 9]. Reasons such as the low photocatalytic activity of TiO_2 under sunlight and rapid

charge recombination that causes a decrease in quantum efficiency reduce the performance of TiO_2 and its utilization as a photocatalyst alone does not produce satisfactory results [9,10].

To bypass these disadvantages and boost the photocatalytic performance of TiO_2, strategies such as surface modification with metal and non-metal elements, combining with other semiconductors, and design of multiple components are applied [11,12]. Recently, the combination of TiO_2 with carbon quantum dots (CQDs) has been a favorite approach to enhance the light-harvesting ability and hence the photocatalytic activity [11]. CQDs are a new category of photoluminescent (PL) carbon nanomaterials with a size of less than 10 nm which consist of the sp^2/sp^3 hybridized carbon atoms carrying different functional surface groups [12]. Currently, CQDs have gained increasing significance owing to their flawless properties such as low toxicity, perfect electron transfer/reservoir characteristics, good up-converted photoluminescence behavior, chemical inertness and superior biocompatibility [6,13,14]. Despite these unique properties of CQDs, their quantum efficiency is limited, and to increase this, doping with heteroatoms has recently attracted much attention [15]. In the literature, it is reported that when nitrogen is added to nanostructured carbon materials, charge delocalization improves, the carbon's work function decreases, and photoluminescence emission capacity effectively increases. These approaches lead to CQDs where they reach unique chemical and physical properties such as tunable electronic and optical properties [16]. Numerous research investigations have employed CQDs/TiO_2 as a photocatalyst for organic pollutant degradation [6-8, 11-15]. However, there remain unresolved queries in this area, particularly regarding the impact of the carbon source material on the photocatalytic efficiency of TiO_2.

Studies exploring the influence of different carbon sources on the photocatalytic performance of TiO_2 are prevalent in the scientific literature. Besides, the utilization of renewable natural resources in the synthesis of CQDs attracts more attention than other synthetic materials because they are environmentally friendly. The synthesis of CQDs, which are used beneficially

in many areas, with simple and environmentally friendly methods without the use of synthetic chemicals, attracts great attention in terms of green chemistry [17]. Chitosan is the *N*-deacetylated derivative of chitin, a renewable natural polysaccharide obtained from crab and shrimp. It is a suitable natural material for the synthesis of CQDs because it involves abundant functional groups of -OH and -NH_2, and is biocompatible, natural and non-toxic. It demonstrates diverse physical characteristics, including viscosity, adhesiveness, and potential solubility in a range of media [17-19]. In existing literature, some studies involve the synthesis of CQDs from chitosan for diverse applications. Ni et al. [20] synthesized an 8-hydroxy-Quinoline-7-carboxylic acid/TiO_2 (HQC/TiO_2) photocatalyst for phenol degradation under visible light illumination and utilized CQDs from chitosan to enhance the dynamic and cyclic stability of HQC/TiO_2. In another study, Midya et al. [21] prepared a photocatalyst through in situ formation and accumulation of TiO_2 NPs and CQDs on the surface of cross-linked chitosan. They used this catalyst in the photooxidation of some organic compounds under solar light and obtained a good photocatalytic performance. However, to the best of our knowledge, there is no research investigating the utilization of CQDs/TiO_2 catalysts fabricated by combining CQDs derived from chitosan with TiO_2 in photocatalytic applications.

Using the above considerations, we fabricated an S-scheme *N*-CQDs/TiO_2 heterojunction photocatalyst for the removal of CIP from water under UVA irradiation. The synthesis of *N*-CQDs/TiO_2 was carried out by hydrothermal method using chitosan as a precursor. Among many methods applied for the synthesis of CQDs, the hydrothermal method is a highly preferred strategy because it is convenient, low-cost, easy and environmentally friendly [22]. Next, the impact of several operational parameters including catalyst concentration, CIP concentration, and initial solution pH on the photocatalytic efficacy of *N*-CQDs/TiO_2 was investigated. A potential photo-oxidation mechanism was proposed based on radical trapping experiments. The catalyst was synthesized through direct contact between TiO_2 nanoparticles and chitosan-

derived *N*-CQDs, without the use of any mediator material. This synthesis approach facilitated exceptional charge separation and transfer, resulting in significantly superior performance compared to pure TiO_2.

2. Materials and Methods

2.1. Fabrication of *N*-CQDs

The synthesis of chitosan-based *N*-CQDs was achieved using an efficient, simple, green, and one-step hydrothermal carbonization method, which is a modified version of the method reported by Hazarika *et al.* [23]. After adding 0.5 g of chitosan to 50 mL of 1M acetic acid, the mixture was agitated for 10 min to produce a translucent sole. After adding 0.3 g of urea, the mixture was subjected to 30 min of ultrasonication (240 W/L of output power, VWR Ultrasonic cleaner USC-THD, China). The reaction mixture was then stirred for 10 min after adding 0.4 mL of glycerol, and for an additional hour after adding 15 mL of 1M HCl. The mixture was transferred to a 100 mL Teflon-lined stainless steel reactor, and it was left to sit at 150 ^{o}C for 6 h. The reactor was cooled to room temperature following carbonization. After being removed from the reactor, the mixture was once more centrifuged (Universal 320 Hettich) at 9000 rpm to separate the solid portion and passed through a 0.45 μm membrane filter. It was then stored in a sealed cap at 5°C for later use in experiments.

2.2. Fabrication of TiO_2

A previously reported method developed by our group was used for the TiO_2 synthesis with minor modifications [7]. The experimental details about the synthesis of TiO_2 are included in the Supporting Information.

2.3. Fabrication of *N*-CQDs/TiO_2

N-CQDs/TiO_2 nanophotocatalyst was prepared by using a five-step protocol as follows. Step 1-Adding 40 mL of water to 10 mL of the *N*-CQDs solution prepared as described above and stirring for 15 min in a magnetic stirrer. Step 2- Dropwise addition of titanium(IV) ethoxide of 1.6 mL to the solution prepared in the first step and mixing in a magnetic stirrer for 1 h. Step 3- Carbonization of the mixture taken into the Teflon lined stainless steel reactor in a muffle oven (Lenton, UK) at 150 ^{o}C for 6 h. Step 4- Separating the suspended *N*-CQDs/TiO_2 nanoparticles taken out of the reactor and washing by centrifuging with ethanol for 10 min at 9000 rpm. Step 5- Drying the nanoparticles obtained in step 4 by heating them at 50 °C for 8 h and storing them in a closed container for subsequent use. The pathway followed while synthesizing the catalyst is schematized in Figure S1.

3. Results and discussion

3.1. Catalyst characterization

The *N*-CQD/TiO_2 heterojunction photocatalyst was fabricated by using a hydrothermal treatment of chitosan biopolymer, as a natural carbon source, in the mixture of glycerol, urea, water and concentrated HCl at 150 ^{o}C for 6h, which is schematized in Figure S1**.** Bare TiO_2 nanoparticles were also prepared by the same strategy without the addition of *N*-CQDs. As-prepared samples were characterized by X-ray diffraction (XRD), transmission electron microscopy (TEM), scanning electron microscope/energy-dispersive X-ray spectroscopy (SEM/EDS), Fourier transform infrared spectroscopy (FT-IR), and X-ray photoelectron spectroscopy (XPS) analyses.

The preparation procedure and compositional variation of the prepared samples were followed by powder XRD analysis. As illustrated in Figure 1 (a), a sharp peak position centered at 22.91° of *N*-CQDs ascribed to the (002) lattice plane of graphite, and the determined interlayer spacing of 0.39 nm was wider than the graphitic interlayer distance (0.32 nm) [24]. The enlargement in

interlayer distance is caused by the formation of more oxygenated functional groups such as -COOH, -OH, and amine groups on the surface and edges of *N*-CQDs during the hydrothermal process [25]. Additionally, the sharp peak at 2θ = 32.62° is attributed to irregular graphite-like *N*-CQDs [26]. The noticeable peak at 2θ = 40.24° (100) can be indexed graphitic sp^2 carbon clusters, while the other peaks at 58.23° (103), and 68.37° (220) signify a diamond-like sp^3 hybridized carbon structure [27]. Moreover, the peaks at 2θ= 46.81° (101) and 52.72° (102) are indexed to the diffraction pattern of graphitic carbon representing conjugated sp^2 carbon scaffolds [24,27,28]. These results are coherent with those previously published for CQDs [27,29,30]. From the XRD diffractogram of TiO_2 (Figure 1b), it was determined that the sample included both rutile and anatase phases, parallel to the outcomes notified by Wang et al [31]. "The distinctive diffraction peaks of TiO_2 at 25.32° (101), 37.39° (004), 48.03° (200), 54.32° (105), 62.75° (204), 68.88° (116), and 77.01° (215) well overlapped with the characteristics diffraction pattern of the anatase phase in the tetragonal crystal structure (JCPDS No. 21-1272) [32,33]. In Figure 1b, the diffraction peaks located at 2θ of 27.53° (110), 36.05°(101), 41.31°(111), 57.12°(220), and 69.79°(301) certified the presence of rutile phase of TiO_2 (JCPDS card 00-21-1276) [34,35]. Additionally, the peak observed at 2θ = 30.80° indicates the brookite phase of TiO_2 (JCPDS No.84-1750) [7]. From the XRD graph of *N*-CQDs/TiO_2 nanocomposites (Figure 1c), only peaks belonging to the anatase phase of TiO_2 were observed. The absence of a rutile phase in the *N*-CQD/TiO_2 nanocomposites can be attributed to the fact that the carbon content prevents a crystal transformation of the crystal phase of TiO_2 to form the rutile phase [6]. The data of XRD revealed that *N*-CQDs were successfully assembled onto TiO_2 surface to yield *N*-CQD/TiO_2 composites. The disappearing of the *N*-CQDs peaks in the XRD difractogram of *N*-CQDs/TiO_2 nanocomposites can be clarified by the weak crystallinity, little quantity, and uniform distribution of *N*-CQDs in the nanocomposite structure [6]. The average crystal sizes were calculated to be 14.88 nm and 8.09 nm for bare TiO_2 and *N*-

CQDs/TiO_2, respectively, by using the Scherrer equation on the anatase (101) diffraction peak at $2\theta = 25.32^{o}$ with a lattice spacing of 0.36 nm [36].

The morphological analyses of the *N*-CQDs and *N*-CQDs/TiO_2 nanocomposites were examined by transmission electron microscope (TEM). The presence of spherical nanoparticles with an average size of ca. 7-8 nm in the TEM image of Figure 2a verifies that *N*-CQDs were successfully synthesized from the chitosan by the hydrothermal method. Figure 2b shows that *N*-CQDs are uniformly disseminated on the surface of TiO_2 particles with a dimension of about 8 nm.

SEM analysis was conducted to examine the surface morphology of *N*-CQDs, bare TiO_2 nanoparticles, and *N*-CQDs/TiO_2 nanocomposites (Figure S2). From the SEM image of *N*-CQDs, it is noteworthy that the *N*-CQDs are partially single and mostly form separate phases as aggregates (Figure S2A and S2B). In Figure S2C, it is seen that there are TiO_2 nanoparticles with aggregated spherical-like shape. Additionally, it was clearly observed that the typical TiO_2 morphology did not change after the introduction of *N*-CQDs into the structure, but it shrinks in size (Figure S2D). This allows the catalyst surface to increase and offers a more reactive area, which is beneficial in photocatalytic degradation. Elemental compositions of as-prepared samples were determined from EDX data (Figure S2E). By using EDX tests, it was determined that the *N*-CQDs sample had 35.39 wt% C, 20,31 wt% O, and 12.57 wt% N; the TiO_2 sample had 51.02 wt% Ti and 48.98 wt% O, and the *N*-CQDs/TiO_2 nanocomposites sample had 4.87 wt% C, 49.14 wt% O, 43.63 wt% Ti, and 0.06 wt% N. These results exhibit clearly the distribution of *N*-CQDs on the TiO_2 surface and the successful fabrication of *N*-CQDs/TiO_2 nanocomposites

The absorption bands and related functional groups in the *N*-CQDs, TiO_2, and *N*-CQDs/TiO_2 samples were investigated using FTIR analysis. The resulting spectra are presented in Figure 3.

In Figure 3a, the FTIR spectrum of *N*-CQDs shows an important peak at 1712 cm^{-1} and a broad peak between 3200 –3600 cm^{-1}, which correspond to C=O and amino groups/O–H stretching vibrations, respectively [37,38]. It can be inferred that the peaks at 1375, 1035, 2802, and 3006 cm^{-1} are responsible for the C–N, C–O, C-H_2 symmetric stretching, and C-H_2 asymmetric stretching vibrations, respectively, while the peak at 3382 may be associated with the N–H vibrations [38,39]. A graphitic assembly and an unsaturated aromatic ring may have formed during the hydrothermal treatment process, according to the stretching vibration peaks of C=C at 1544 cm^{-1} [38]. The distinct peaks at 1255 cm^{-1}, 1442 cm^{-1}, and 1375 cm^{-1} correspond to the stretching vibration modes of C-N heterocycles, whereas the peak at 3228 cm^{-1} represents the NH stretching vibrations [38]. The absorption band at 2943 cm^{-1} was assumed to be the asymmetric stretching vibration of –CH_2 [39,40]. According to FT-IR results, hydrophilic functional groups like -COOH, -NH_2, and -OH coated the surface of *N*-CQDs. Additionally, it implied that it had something to do with the exceptional solubility of *N*-CQDs in solution. FT-IR spectra of TiO_2 and *N*-CQDs/TiO_2 are shown in Figures 3b and 3c, respectively. Both samples exhibit a broad absorption band below 1000 cm^{-1}, which is indicative of the Ti-O-Ti bond's vibration. The O-H stretching vibration of the adsorbed water on the sample surfaces is responsible for the broad absorption band observed approximately at 3200 cm^{-1} and Ti-OH bending vibrations was observed at 1623 cm^{-1} for the two samples [41]. The bonds of C-O-C, Ti-O-C, and Ti-O-Ti are responsible the intense peaks of *N*-CQDs at 1000–1400 cm^{-1}, the peak of *N*-CQDs/TiO_2 at 1060 cm^{-1}, and the bands at 1066 and 1410 cm^{-1} for TiO_2, respectively [41,42]. These findings supports the XPS results. Furthermore, compared to bare TiO_2, it was found that the broad absorption band below 1000 cm^{-1} widened and shifted toward high wavenumber in the FTIR spectra of *N*-CQDs/TiO_2 nanocomposite. This behavior was linked to a combination of Ti-O-Ti and Ti-O-C vibrations, indicating that the Ti-O-C bond formation is responsible for the coupling between bare TiO_2 and *N*-CQDs [41,43]. The movement of the

absorption band appeared at 611.39 cm^{-1} in the FT-IR spectra of TiO_2, resulting from the Ti-O vibration, to 611.37 cm^{-1} in *N*-CQDs/TiO_2 clearly approves that carbonaceous groups were incorporated on the surface of TiO_2 [7].

Surface chemical composition in the prepared *N*-CQDs and *N*-CQDs/TiO_2 nanocomposite and the interaction between *N*-CQDs and TiO_2 were analyzed by the X-ray photoelectron spectroscopy (XPS) as displayed in Figure S3 (a, b) and Figure 4(a-c). According to the XPS survey spectrum shown in Figure S3a, *N*-CQDs sample involves C, O, and N elements with located binding energy peaks at 285.08, 532.08, and 401.05 eV, respectively, revealing the successful synthesis of *N*-CQDs by the hydrothermal method. In the XPS survey spectrum of *N*-CQDs/TiO_2 (Figure S3a), there are the peaks at 285.07, 398.08, 458.08 and 530.09 eV belong to C 1s, N 1s, Ti 2p, and O 1s, indicating the introduction of *N*-CQDs into the TiO_2 structure. The high-resolution XPS spectrum of the N 1s region shows a peak at 401.05 eV (Figure S3b) that can assigned to the pyridine groups that have powerful electron giving potential and provide excellent catalytic performance in redox reactions [14]. In the C 1s deconvoluted spectra of *N*-CQDs (Figure 4a), the peaks at 284.5, 286.1, and 288.4 eV are assigned to C-C/C=C, C-N/C-O, and C=N/C=O bonds, respectively [44,45]. In the high-resolution C 1s spectrum of *N*-CQDs/TiO_2 nanocomposites given in Figure 4(a), it was seen that the binding energy of the C 1s peaks changed to 284.5, 285.7, and 287.9 eV, respectively. This change in binding energies of C 1s peaks may indicate that the interaction between TiO_2 and *N*-CQDs occurs through Ti-O-C bonds formed between the C=O bonds in *N*-CQDs and Ti-O bonds in TiO_2 [14, 45]. For the pristine TiO_2 (Figure 4b), the deconvolution of the Ti 2p signal was fitted into two peaks at 457.8, and 463.7 eV, assigning to the Ti $2p_{3/2}$ and Ti $2p_{1/2}$ core levels of Ti^{4+} species, respectively, depicting a characteristic spin-orbital doublet splitting of 5.7 eV [45,46]. It was observed that these binding energies shifted to 458.2 and 463.9 eV in the *N*-CQD/TiO_2 nanocomposites, suggesting that TiO_2 and *N*-CQDs may interact through the formation of Ti-

O-C bonds [14]. In addition, in the high-resolution O 1s spectrum of *N*-CQDs (Figure 4(c)), two peaks located at 531.2 eV and 532.4 eV indicate the presence of C=O and C-O bonds [45]. The O1 s spectrum of pristine TiO_2 in Figure 4c presents two pronounced peaks positioned at 529.1 eV, and 531.4 eV, which could be imputed to Ti-O, and C-O-H, respectively [46]. For *N*-CQDs/TiO_2, the binding energies associated with these bonds shifted to the higher energy area at 529.45 eV and 531.59 eV, respectively. Compared with pristine TiO_2, the binding energy of Ti-O-bond in *N*-CQD/TiO_2 nanocomposite shifts towards the higher energy region, approving that there is a charge transfer between TiO_2 and *N*-CQDs (Figure 4c) [46].

The textural properties and porosity of the prepared *N*-CQDs, TiO_2 and *N*-CQDs/TiO_2 nanocomposites were examined by the Brunauer-Emmett-Teller (BET) method. Figure S4A displays the nitrogen adsorption-desorption isotherms of *N*-CQDs, TiO_2 and *N*-CQDs/TiO_2 nanocomposites and their related Barrett-Joyner-Halenda (BJH) pore size distribution curves illustrated in Figure S4B, and Table S2 summarizes the detailed textural properties of the catalysts. Concerning the IUPAC classification, all of the adsorption isotherms are of type IV isotherm exhibiting mesoporous character [47]. Incidentally, *N*-CQDs/TiO_2 showed an H2-type hysteresis loop in p/p^0 of 0.4–0.80, which corresponds to a wide pore size distribution or pores with narrow necks and wide bodies, entitled ink bottle pores [47-50]. The isotherms belonging to TiO_2 and *N*-CQDs presented a Type H3 hysteresis loop, which does not exhibit limiting adsorptions at high p/p^o values, implying the existence of slit-shaped pores [50]. The shifting of the inflection point to lower pressures for *N*-CQDs/TiO_2 nanocomposites compared to that of TiO_2 means that there is a decrease in pore size as a result of *N*-CQDs incorporation into the TiO_2 structure [49], which was evidenced by the pore size distribution of the same samples as represented in BJH plot and Table S2. This implies that there are strong interactions between *N*-CQDs and TiO_2 nanoparticles. As can be seen from Table S2, the BET surface areas of TiO_2, *N*-CQDs, and *N*-CQDs/TiO_2 photocatalysts were estimated to be 71.798, 1.091, and 213.792

m^2/g. This might be probably attributed to the shrinkage of the crystal size of TiO_2 as supported by XRD and TEM results and the formation of narrow pores as a result of the arrangement in the pore structure with the introduction of *N*-CQDs into the TiO_2 structure. Pore volumes of catalysts in the same order were found as 0.186, 0.003, and 0.203 cm^3/g. On the contrary, the mean pore diameter of *N*-CQDs/TiO_2 (3.210 nm) was much narrower than that of the TiO_2 (9.524 nm) and *N*-CQDs (5.171 nm). The increase in pore volume and surface area of *N*-CQDs/TiO_2 compared to TiO_2 means more active centers, which helps to raise the CIP concentration of *N*-CQDs/TiO_2 surface, simplifying the reaction between ROS species and CIP molecules [51,52]. Because in photocatalytic processes, adsorption occurs before degradation, which requires a high surface area [52]. However, it cannot be said that there is a direct relationship between the improved photocatalytic efficiency and the surface area [52]. The adsorption of the pollutant, together with its degradation products and ROS species, to the catalyst's surface is the initial stage in heterogeneous photocatalytic reactions. Therefore, the catalyst's surface area plays a crucial role in supplying active centers that are appropriate for adsorption. However, since there won't be any accumulation on the catalyst surface, there is no direct correlation between the size of the catalyst surface and the removal effectiveness because the rate at which ROS species degrade pollutant molecules is higher than the rate at which they adsorb them. It is crucial that ROS species arise without charge carrier recombination and that redox reactions take place between these species and pollution molecules.

The effectiveness of a photocatalyst significantly depends on its ability to harvest light and prevent charge recombination, and its efficiency in charge separation. Therefore, UV–Vis-NIR DRS measurements of *N*-CQDs, TiO_2 and *N*-CQDs/TiO_2 nanocomposites were performed, band gaps were calculated, and photoluminescence spectra were obtained to evaluate the improvement in the photocatalytic activity of TiO_2 with the introduction of *N*-CQDs into TiO_2 structure. The results are collectively presented in Figure 5. As demonstrated in Figure 5a, TiO_2

absorbs only in the UV region, while *N*-CQDs/TiO_2 absorbs in both the UV and visible region due to the presence of *N*-CQDs whose absorption band is red-shifted. The shifting of the absorption edge of *N*-CQDs/TiO_2 (423 nm) to the more visible region compared to that of TiO_2 (373 nm) can be attributed to the chemical interactions of TiO_2 and *N*-CQDs through the Ti-O-C bonds. Possible interactions in the *N*-CQDs/TiO_2 nanocomposites affect the interfacial transport rate of e^-/h^+ pairs, which is highly beneficial for catalytic activity [51,53]. Figure 5b shows the absorption spectrum and band gap energy of *N*-CQDs (the inset graph). The typical peak at 350 nm resulting from the n → π* transition of the C=O bond and other functional groups reveals that the synthesis of *N*-CQDs has been successfully achieved which was similar to other published reports of *N*-CQDs [54-56].

Band gap energy (Eg) of the *N*-CQDs, TiO_2 and *N*-CQDs/TiO_2 nanocomposites was estimated by using the Tauc formula (Eq.1) [51, 52].

$$(\alpha h\nu)^2 = A(h\nu - E_g) \quad (1)$$

here; h, ν, α, Eg and A symbolize the Planck constant, frequency of vibration, absorption coefficient, band gap, and a proportional constant, respectively. The estimated bandgap values of the samples are given in Figures 5b and 5c. The E_g values of *N*-CQDs, pristine TiO_2 and *N*-CQDs/TiO_2 nanocomposites were computed to be 1.91, 3.32, and 2.93 eV, respectively. The reduction of the band gap from 3.32 eV to 2.93 eV reveals that the *N*-CQDs/TiO_2 nanocomposites could benefit from all wavelengths and accordingly, its photocatalytic activity will be higher than TiO_2 [51].

For a better understanding of the role of *N*-CQDs on the capability of effectual charge transport and separation in *N*-CQDs/TiO_2 photocatalyst, the PL spectra of the *N*-CQDs, TiO_2, and the *N*-CQDs/TiO_2 nanocomposites were recorded with an excitation wavelength of 325 nm at room temperature. *N*-CQDs exhibit the most powerful PL emission spectrum centered at 539.5 nm.

After coupling with TiO_2 nanoparticles, *N*-CQDs/TiO_2 nanocomposites displayed the weakest PL intensity (Figure 5d), attributing to the limited recombination of photogenerated e^-/h^+ pairs, probably due to the formation of binary heterojunction between *N*-CQDs and TiO_2 [51,57].

3.2. Comparison of different processes on the CIP removal

In order to evaluate the contribution of each process to CIP elimination in the *N*-CQDs/TiO_2/ aqueous CIP solution system, several experiments were performed under predetermined optimum conditions, as 10 mg/L CIP, 0.4 g/L catalyst and the pH of 5 (natural pH). Figure 6a illustrates the results of a comparative study on CIP removal. As can be seen from the Figure 6a, the single application of adsorption and photolysis (UVA) processes for CIP removal resulted in CIP removal of 3.38% and 10.58% after 120 min irradiation time, respectively. In other words, these treatment methods were insufficient in removing CIP due to the lack of adsorption capacity of *N*-CQD/TiO_2 photocatalyst or unsatisfactory free radical production via UVA irradiation. On the other hand, the performance of the TiO_2/UV was importantly higher than alone UVA irradiation and attained 41.14% CIP removal, revealing the efficient role of TiO_2 as a catalyst which contributes to the production of free radicals through the photocatalytic process. When TiO_2 was combined with *N*-CQDs, 83.91% of CIP removal was achieved. The higher degradation of CIP by using *N*-CQDs/TiO_2 photocatalyst compared to TiO_2 catalyst, displays that the combination of TiO_2 with *N*-CQDs can improve the photocatalytic activity under UVA irradiation. This enhancement in the presence of *N*-CQDs, which is attributed to the charge transfer occurring at the interface between *N*-CQDs and TiO_2, leads to the improved photocatalytic efficiency of the *N*-CQDs/TiO_2 nanocomposites and enhances the CIP degradation [8].

The carbon content of the composite is important in the photocatalytic performance of semiconductors equipped with *N*-CQDs. The appropriate amount of carbon for the *N*-

CQDs/TiO_2 catalyst was found by keeping the TiO_2 ratio constant and changing the *N*-CQDs amounts. Figure 6b shows the results obtained from the experiments. As seen from Figure 6b, the removal efficiencies for 0, 0.09, 0.12, 0.18 and 0.25 g of *N*-CQDs were found to be 41.14%, 59.12%, 83.91%, 71.27%, and 50.24%, respectively. It is understood from the results that the best charge transfer was obtained by using 0.12 g of *N*-CQDs. When there is an appropriate proportion of *N*-CQDs in the composite, *N*-CQDs uniformly distributed on the TiO_2 surface act as both acceptors and donors to create a new electric field. In this way, the charge carriers are separated, the recombination tendency is reduced, and redox reactions of nanocomposites are stimulated by e^-/h^+ pairs, therefore, it causes an increase in ROS species, which increases CIP removal. On the other hand, *N*-CQDs increase the light absorption of TiO_2 nanoparticles due to their spectral properties, which increases CIP removal efficiency. Moreover, *N*-CQDs provide active centers suitable for adsorption, resulting in an increase in the amount of adsorbed species [41,57]. Increasing the amount of *N*-CQDs above 0.12 g caused a decrease in the CIP removal efficiency. In this case, the excess *N*-CQDs compete with TiO_2 to absorb the incident light. Moreover, by burying a large part of the TiO_2 surface under *N*-CQDs, the photoexcitation of TiO_2 decreases and the photocatalytic efficiency of the catalyst decreases because the amount of charge carriers decreases. Additionally, an excess of *N*-CQDs causes light scattering. On the other hand, the abundance of *N*-CQDs acts as recombination centers for light-induced e^-/h^+ pairs. All these result in decreased photocatalytic activity [41,58]. The experimental data obtained for each process were applied to the pseudo-first-order model using the following equation [7].

$$ln\frac{A_0}{A} = k_{app}t \quad (2)$$

$$t_{1/2} = \frac{\ln 2}{k_{app}} \quad (3)$$

Here; A_0 and A_t denoted the CIP absorbance value before photocatalytic oxidation and after some certain time (min), respectively, k_{app} is rate constant (apparent), and t is the time [57,58]. The fitted first-order equation-related kinetic parameters of the experimental data, namely k (min^{-1}) and R^2, together with the calculated $t_{1/2}$ (min) are shown in Figure 6c. The analysis results showed that CIP removal conformed to the pseudo first-order kinetic model for all of the processes. The photocatalytic process using *N*-CQDs/TiO_2 nanocomposites with the highest k_{app} (0.0138 min^{-1}) and lowest $t_{1/2}$ (50.23 min) is considered the best-performing process [7].

It is obvious that doping with *N*-CQDs plays a major role in the performance of the *N*-CQDs/TiO_2 in CIP removal. However, in order to see the effect of the carbon source on the performance of *N*-CQDs, we prepared the *N*-CQDs from glucose using the same conditions described for the chitosan one. When the CIP removal was examined under the same conditions, 39% removal efficiency in 120 min was obtained with the catalyst prepared from glucose. The fact that the *N*-CQDs/TiO_2 nanocomposites prepared with *N*-CQDs obtained from chitosan show a much higher performance than the catalyst prepared from glucose may be due to the different functional groups, and chain length that the two sources possess [59]. This can be explained by the fact that *N*-CQDs generated from chitosan, as opposed to those derived from glucose, have richer surface functional groups due to the presence of N groups, which enhance CIP adsorption and encourage photocatalytic activity. Upon this result, it was concluded that chitosan is a suitable precursor for the synthesis of *N*-CQDs.

3.3. Effect of operational parameters on the photocatalytic degradation of ciprofloxacin in the presence of *N*-CQDs/TiO_2 nanocomposites

3.3.1. Catalyst amount

To find the optimum catalyst dosage value in photocatalytic oxidation of CIP, the experiments were conducted at varying catalyst concentrations in the range of 0.05 g/L - 0.6 g/L, while

other operational parameters are constant (CIP concentration of 10 mg/L, and pH 5). As revealed in Figure S5, CIP degradation efficiency increased from 42.58 % to 83.91 % in 120 min by increasing catalyst concentration from 0.05 g/L to 0.40 g/L and decreased thereafter. The enhancement in degradation efficiency can be explained by the higher reachable reaction centers in the *N*-CQDs/TiO_2 surface and more generated free radicals that are available for CIP degradation. It can be said that above the catalyst concentration of 0.4 g/L, a possible catalyst agglomeration, resulting in a reduction of the active sites of the catalyst in solution, leads to a decrease in photocatalytic activity [60]. In addition, the increase in turbidity of the solution in over dosage of the catalyst leads to a decrease in the penetration of light through the solution, resulting in lower photocatalytic degradation [61]. Based on the outcomes, a concentration of 0.4 g/L of *N*-CQDs/TiO_2 catalyst was selected in all the remaining steps of this study.

3.3.2. Influence of initial concentration of CIP

In the photocatalytic process, the concentration of wastewater contaminated with antibiotics is an important parameter in pollution removal. To examine the effect of the concentration of CIP was taken in the range of 5-25 mg/L in the study. At all concentrations, the degradation efficiency of CIP was found to increase with increasing time (Figure S6). According to Figure S6, for the residence time of 120 min, the degradation efficiency increased from 38.44 % to 91.8 % by reducing the initial CIP concentration from 25 to 5 mg/L. The decrease in removal efficiency as CIP concentration increases can be attributed to the following reasons. One is that the fixed amount of ROS species produced by a unit amount of catalyst is not enough to degrade the increasing concentration of CIP. Second, a concentrated pollutant solution can prevent *N*-CQDs/TiO_2 particles from absorbing erased UV-A waves [57,62].

3.3.3. Impact of pH

Initial solution pH is an important parameter that has an influence on the pollutant ionization

degree, surface charge of catalyst, radical production and interfacial potential in AOPs [63]. Therefore, the effect of variation in the solution pH on the CIP degradation efficiency in the existence of *N*-CQDs/TiO_2 photocatalyst was researched and zeta potentials of solid particles in catalyst/water suspensions were measured at different initial pHs (2, 3, 4, 5, 6, 8, 9, and 10). The results are given in Figure S7a and S7b. As clearly seen from Figure S7a, the CIP degradation efficiencies of 19.28 %, 41.75 %, 55.02 %, 83.91 %, 61.93 %, 64.28 %, 65.71 %, and 60.92 % were obtained for the respective pH values of 2, 3, 4, 5, 6, 8, 9 and 10 for the elapsed time of 120 min. The value of pH_{zpc} (zero point of charge) for *N*-CQDs/TiO_2 photocatalyst was determined to be 6.6 (Figure S7b). That is, below and above the pHzpc, the surface of the catalyst is positively and negatively charged, respectively. CIP has two pKa values (5.9 and 8.89), and is present in aqueous solution as a cation ($CIP^{0,+)}$ below pH 5.9, as a zwitter ion ($CIP^{-,+}$) between pH 5.9 and pH 8.89, and as an anion($CIP^{-,0}$) above pH 8.89 [61,64]. As can be understood from Figure S7a, the highest percentage degradation of CIP was obtained at pH 5 (natural pH of CIP), and then decreased. The low degradation efficiency observed at values below pH 5 can be ascribed to the repulsive forces between the CIP molecules and the catalyst particles, both of which are positively charged, and the scavenger effect of Cl^- ions from the HCl used to adjust the pH of the solution. Although both catalyst and CIP molecules are positively charged at pH 5, the high degradation efficiency observed can be attributed to the CIP adsorption by hydrogen bonds between the carboxyl, ketone, amine, and F groups of CIP molecules and the catalyst molecules. It can be said that the presence of repulsive forces between catalyst particles whose surface becomes negative and CIP molecules causes a gradual decrease in CIP degradation after pH 5, resulting in low photocatalytic activity. Considering the reasons explained above, all experiments in this study were carried out at pH 5, which is the natural pH value of the CIP solution.

3.4. Band alignments

Prior to proposing a plausible mechanism for any photodegradation mechanism, define the band edges of the components within the constructed heterojunction. To satisfy this requirement, analytical methods such as valence band (VB) - XPS analyses and Tauc plots achieved this precise determination of photophysical features. The VB-XPS-measured valence band (VB) potentials, as illustrated in Figure S8a and S8b, are identified where the tangent and oblique lines near the X-axis intersect at a point. The energy values of 2.55 eV for *N*-CQDs and 1.70 eV for TiO_2 were extracted from the intersection of these critical findings and then standardized to the standard hydrogen electrode potential ($E_{VB\text{-}NHE}$) using a well-known formula [65].

$$E_{VB-NHE} = \Phi + E_{VB-XPS} - 4.44 \quad (4)$$

Here, E_{NHE}, Φ, and $E_{VB\text{-}XPS}$ stand for the standard electrode potential, the XPS analyzer's work function that is herein used, and the VB is the value obtained from VB-XPS analysis, respectively [66]. Utilizing this formula, VB values of 2.55 V for *N*-CQDs and 1.70 V for TiO_2 were ascertained. Upon combining the VB-XPS and Tauc plot outcomes, it was evident that the conduction bands (CB) of *N*-CQDs and TiO_2 are positioned at 0.64 V and -1.62 V, respectively, as graphically depicted in Figure S8c.

Investigating the photodegradation mechanism of CIP calls for an in-depth exploration of charge transfer dynamics at the interfaces between its components, a parameter of profound importance alongside band alignments. The functional roles of these band edges become clearer through the work functions of pristine materials obtained from both experimental and theoretical analyses. Using VB-XPS, we determined work function values for *N*-CQDs, TiO_2, and the *N*-CQDs/TiO_2 composite, as illustrated in Figure 7a-c. When materials meet at their interfaces, the degree of the work function largely dictates the direction of the generated charge transfer. A greater work function value signifies that the Fermi level is more distant from the vacuum level, facilitating the acceptance of electrons by a material with a lower work function. Consequently, during this charge transfer, one component's surface becomes positively charged

while the other becomes negatively charged [67]. We determined the work function of each element by utilizing the specified equation

$$\Delta V = \Phi - \varphi \quad (5)$$

Φ is the work function of material and φ is the work function of the device that is used (4.543 eV) [68]. The binding energy gap, ΔV, can be calculated between the inflection points (IP1; a point at which the alteration in binding energy commences at the reference level and IP2; a midpoint of Fermi Energy distribution) [69]. As a result, the values of 7.52, 6.83, and 7.14 eV were obtained for *N*-CQDs, TiO_2, and *N*-CQDs/TiO_2, respectively (Figure 7a-c).

Upon interface formation, TiO_2 with a lower work function compared to *N*-CQDs, becomes conducive to electron donation. Consequently, *N*-CQDs accept electrons until the Fermi level reaches equilibrium. An internal electric field (IEF) is generated via this charge distribution at the interfaces, leading to an upward bending of TiO_2's band edges and a downward bending of *N*-CQDs' band edges, as depicted in Figure 7d [70]. This spatial mismatch results in a difference in CB and VB between *N*-CQDs and TiO_2, facilitating the necessary charge separation [71]. During UVA irradiation, the recombination of photo-generated electrons in CB of *N*-CQDs and holes in VB of TiO_2 is facilitated by the IEF and band bending. This allows electrons in TiO_2's VB and holes in *N*-CQDs'CB to migrate easily, fostering the interfacial connection. Consequently, a characteristic S-scheme heterojunction form aids in photo-generated charge separation through the dynamic redistribution of charge carriers around the heterogeneous interface [72]. These findings align with the superior photocatalytic activity of *N*-CQDs/TiO_2, highlighting their exceptional charge separation characteristics.

3.5. Effect of various scavengers

Photogenerated holes (h^+), hydroxyl radicals ($OH^\bullet$), and superoxide radicals $O_2^{-\cdot}$ are the main ROS involved in the photocatalytic degradation of pollutants [73]. In order to find out the

contribution of these ROS species to the photocatalytic degradation of CIP in the *N*-CQDs/TiO_2/CIP solution system, experiments were carried out with some selected scavengers under optimum conditions. The obtained results are illustrated in Figure S9. The ratio of CIP to scavenger was kept constant at 1:1 in the experiments. For this purpose, various scavengers agents, such as isopropanol (IPA), benzoquinone (BQ), potassium iodide (KI), sodium oxalate ($Na_2C_2O_4$), and EDTA-Na_2 were added to the reaction solution to act as a h^+ and $OH^{\bullet}_{free}$ radical scavenger, $O_2^{-\cdot}$ radical scavenger, $OH^{\bullet}_{free}$ and $OH^{\bullet}_{surface}$ radical scavenger, and h^+ scavenger, respectively [52, 73,74]. As seen in Figure S9, after 120 min, the percentage degradation of CIP was reduced from 83.91 % to 66.04 %, 49.07 %, 41.40 %, 31.04 % and 27.59 % in the existence of IPA, BQ, KI, $Na_2C_2O_4$, and EDTA-Na_2, respectively. When the results obtained from the experiments are taken into account, it is understood that the ROS sequence that is effective in CIP degradation is $h^+ > OH^{\bullet}_{surface} > O_2^{-\cdot}$.

Considering the results of the experiments performed so far, the proposed mechanism for the improved charge separation and increased photocatalytic activity of the *N*-CQDs/TiO_2 photocatalyst is presented in Figure 8. The coupling, which occurs by hybridization of the conduction band of TiO_2 with the π electrons of *N*-CQDs, reduces the bandgap energy of the composite formed compared to TiO_2 and provides more radiation absorption than TiO_2, due to the newly developed energy levels. These energy levels allow the *N*-CQDs to act as a very good electron acceptor [75]. In addition to increasing the light absorption capacity, the use of the maximum band potential of the nanocomposite with the S-scheme mechanism provides effective charge separation and enables the necessary redox reactions to occur. As seen in Figure 7d, the electrons produced by *N*-CQDs with UVA rays recombine with the photogenerated holes of TiO_2. Thus, while photooxidation reactions occur in the CB of *N*-CQDs, photoreduction reactions occur in the VB of TiO_2.

Possible reactions during CIP degradation are given below.

$$N - CQDs/TiO_2 + h\nu \rightarrow e^- + h^+ \quad (6)$$

After the formation of the photogenerated e^-/h^+ pair, O_2 molecules adsorbed in the CB of TiO_2 capture the photogenerated electrons and form superoxide radicals ($O_2^{\cdot-}$).

$$O_2 + e^- \rightarrow O_2^{\cdot-} \quad (7)$$

CIP molecules are degraded by $\cdot O_2^-$ radicals, but since they are unstable in aqueous solution, superoxide radicals that cannot interact with CIP molecules are converted into $OH^\bullet$ radicals according to the following reactions (Eqs.of 8 and 9) [76].

$$O_2^{\cdot-} + 2H^+ + e^- \rightarrow H_2O_2 \quad (8)$$

$$H_2O_2 + e^- \rightarrow OH^\bullet{}_{surface} + OH^- \quad (9)$$

According to the results of the trapping experiments, since adsorbed $OH^\bullet$ radicals are more effective in CIP degradation, the $OH^\bullet$ radicals formed are adsorbed on the surface of the catalyst and degrade the CIP molecules. On the other hand, holes (h^+) in the valence band of *N*-CQDs directly destroy CIP molecules or combine with H_2O and turn into $OH^\bullet$ radicals.

$$h^+ + CIP \rightarrow Degradation\ products \rightarrow CO_2 + H_2O \quad (10)$$

$$h^+ + H_2O \rightarrow OH^\bullet + H^+ \quad (11)$$

$$OH^\bullet{}_{surface} + CIP \rightarrow OH^\bullet + H^+ \quad (12)$$

$$O_2^{\cdot-} + CIP \rightarrow Degradation\ products \rightarrow CO_2 + H_2O \quad (13)$$

In order to compare the results of the present study with previous studies of CIP degradation using various catalysts, the findings are presented in Table S3 considering the concentration, reaction time and the CIP degradation efficiency. When compared with the results of the studies

reported in Table S3, it is understood that the presented *N*-CQDs/TiO_2 photocatalysts showed good performance in CIP removal under the studied conditions.

4. CONCLUSIONS

N-CQDs prepared by a simple green hydrothermal technique were anchored to TiO_2 nanoparticles surface to yield *N*-CQDs/TiO_2 binary heterojunction for improving the photocatalytic performance of pristine TiO_2. The comprehensive characterization studies revealed that *N*-CQDs with an average size of 7-8 nm were successfully incorporated into the TiO_2 nanoparticles structure and *N*-CQDs/TiO_2 binary heterojunction were successfully fabricated. As-prepared *N*-CQDs/TiO_2 heterojunction photocatalysts exhibited a good performance in the photodegradation of CIP in aqueous solution under UVA radiation. Detailed studies disclosed that the *N*-CQDs amount in *N*-CQDs/TiO_2 nanocomposite had an important effect on photocatalytic CIP oxidation, with the best-selected combination being pH 5 (natural CIP pH), 0.4 g/L catalyst dose, and 10 mg/L CIP concentration where the produced ROS species during photocatalysis played an active role for the CIP degradation in the sequence of $h^+ > OH^{\bullet}_{surface} > O_2^{-\cdot}$. Under the predetermined optimum conditions, 83.91% CIP removal in 120 min was achieved. The kinetic analysis results showed that CIP removal conformed to the pseudo-first-order kinetic model. The increased photocatalytic activity of *N*-CQDs/TiO_2 photocatalysts compared to pristine TiO_2, thanks to the formation of the S-scheme heterojunction structure, allows the interface formed between *N*-CQDs and TiO_2 to support electron transport, increased light absorption ability resulting from the quantum size effect, and to the reduced tendency to resist charge transfer may be attributed. This work recommends an applicable approach for the fabrication of S-scheme heterojunction via the formed strong interaction such as Ti-O-C. The high-performance of *N*-CQDs/TiO_2 photocatalysts sheds new light on the design of efficient photocatalysts for the removal of CIP and similar organic contaminants.

ACKNOWLEDGMENTS

The authors would like to express special thanks to Atatürk University for the financial support (Project of FHD-2021-8950) and the East Anatolia High Technology Application and Research Center (DAYTAM) for technical support for the materials characterization. Y.A. thanks to the Council of Higher Education (YOK/100–2000). This work is a chapter in the Ph.D. thesis of YA. Ö.M. thanks to Turkish Academy of Science (TUBA) for the partial financial support (Grant No: 2023).

References

[1] Liu C, Zhu C, Wang H, Xie S, Zhou J et al. Synergistic removal of organic pollutants by Co-doped MIL-53(Al) composite through the integrated adsorption/photocatalysis. Journal of Solid State Chemistry 2022; 316 (123582). https://doi.org/10.1016/j.jssc.2022.123582

[2] Chang X, Meyer MT, Liu X, Zhao Q, Chen H et al. Determination of antibiotics in sewage from hospitals, nursery and slaughter house, wastewater treatment plant and source water in Chongqing region of Three Gorge Reservoir in China. Environmental Pollution 2010; 158 (5):1444–1450. https://doi.org/10.1016/j.envpol.2009.12.034

[3] Hassani A, Karaca M, Karaca S, Khataee A, Acisli O et al. Preparation of magnetite nanoparticles by high-energy planetary ball mill and its application for ciprofloxacin degradation through heterogeneous Fenton process. Journal of Environmental Management, 2018; 211: 53–62. https://doi.org/10.1016/j.jenvman.2018.01.014

[4] Diao ZH, Xu XR, Jiang D, Li G, Liu J.J et al. Enhanced catalytic degradation of ciprofloxacin with FeS_2/SiO_2 microspheres as heterogeneous Fenton catalyst: Kinetics, reaction pathways and mechanism. Journal of Hazardous Materials 2017; 327: 108–115. https://doi.org/10.1016/j.jhazmat.2016.12.045

[5] Açışlı Ö. Photocatalytic activity of natural ground hematite in heterogeneous photo-Fenton process. Desalination and Water Treatment 2019;167:200-211. https://doi.org/10.5004/dwt.2019.24631

[6] Zhang J, Liu Q, Wang J, He H, Shi F et al. Facile preparation of carbon quantum dots/TiO_2 composites at room temperature with improved visible-light photocatalytic activity. Journal of Alloys and Compounds 2021; 869: 159389 https://doi.org/10.1016/j.jallcom.2021.159389

[7] Karaca M, Eroğlu Z, Açışlı Ö, Metin Ö, Karaca S. Boosting Tetracycline Degradation with an S-Scheme Heterojunction of N-Doped Carbon Quantum Dots-Decorated TiO_2. ACS Omega 2023; 8(29): 26597–26609. https://doi.org/10.1021/acsomega.3c03532

[8] Kumar MS, Yasoda KY, Kumaresan D, Kothurkar NK, Batabyal SK. TiO_2-carbon quantum dots (CQD) nanohybrid: enhanced photocatalytic activity. Materials Research Express 2018; 5(7): 075502. https://doi.org/10.1088/2053-1591/aacbb9

[9] Chen J, Qiu F, Xu W, Cao S, Zhu H. Recent progress in enhancing photocatalytic efficiency of TiO2-based materials. Applied Catalysis A: General 2015; 495: 131-140. https://doi.org/10.1016/j.apcata.2015.02.013

[10] Nasr M, Eid C, Habchi R, Miele P, Bechelany M. Recent Progress on Titanium Dioxide Nanomaterials for Photocatalytic Applications. ChemSusChem. 2018;11: 3023-3047. https://doi.org/10.1002/cssc.201800874.

[11] Deng Y, He R, Lu H, Guo Y, Wang Q et al. Visible-light driven and efficient photoelectrochemical aptasensor constructed with N-doped carbon quantum dots-decorated TiO_2 nanorods for determination of di-2-ethylhexyl phthalate. Chemical Engineering Journal 2023; 468:143583. https://doi.org/10.1016/j.cej.2023.143583

[12] Makama AB, Umar M, Saidu SA. CQD-Based Composites as Visible-Light Active Photocatalysts for Purification of Water. Visible-Light Photocatalysis of Carbon-Based Materials 2018. https://www.intechopen.com/chapters/59867

[13] Miao R, Luo Z, Zhong W, Chen SY, Jiang T et al. Mesoporous TiO_2 modified with carbon quantum dots as a high-performance visible light photocatalyst. Applied Catalysis B: Environmental 2016; 189:26-38. https://doi.org/10.1016/j.apcatb.2016.01.070

[14] Wei N, Yang J, Miao J, Jia R, Qin Z. Production of the protein-based nitrogen-doped carbon quantum dots/TiO_2 nanoparticles with rapid and efficient photocatalytic degradation of hexavalent chromium. Journal of Photochemistry and Photobiology A: Chemistry 2023; 444:114947. https://doi.org/10.1016/j.jphotochem.2023.114947

[15] Tang J, Zhang Y, Kong B, Wang Y, Da P et al. Solar-driven photoelectrochemical probing of nanodot/nanowire/cell interface. Nano Letters 2014; 14 (5): 2702 – 2708. https://doi.org/10.1021/nl500608w

[16] Zhang J, Zhang X, Dong S, Zhou X, Dong S. N-doped carbon quantum dots/TiO_2 hybrid composites with enhanced visible light driven photocatalytic activity toward dye wastewater degradation and mechanism insight. Journal of Photochemistry and Photobiology A: Chemistry 2016; 325: 104–110. https://doi.org/10.1016/j.jphotochem.2016.04.012

[17] Liu X, Pang J, Xu F, Zhang X. Simple approach to synthesize amino-functionalized carbon dots by carbonization of chitosan. Scientific Reports 2016; 6: 31100. https://doi.org/10.1038/srep31100

[18] Rafiee F, Tajfar N, Mohammadnejad M. The synthesis and efficiency investigation of a boronic acid-modified magnetic chitosan quantum dot nanocomposite in the detection of Cu^{2+} ions. International Journal of Biological Macromolecules 2021; 189:477-482. https://doi.org/10.1016/j.ijbiomac.2021.08.158

[19] Oliveira BP. de, Bessa NU. de C, do Nascimento JF, de Paula Cavalcante CS, Fontenelle RO. dos S et al. Synthesis of luminescent chitosan-based carbon dots for Candida albicans bioimaging. International Journal of Biological Macromolecules 2023; 227:805-814. https://doi.org/10.1016/j.ijbiomac.2022.12.202

[20] Ni D, Shang Q, Guo T, Wang X, Wu Y et al. An effective strategy to improve dynamic and cyclic stability of HQC/TiO_2 photocatalyst by introducing carbon quantum dots or iron ion via metal-complex. Applied Catalysis B: Environmental 2017; 210:504-512. https://doi.org/10.1016/j.apcatb.2017.04.019

[21] Midya L, Sarkar AN, Das R, Maity A, Pal S. Crosslinked chitosan embedded TiO_2 NPs and carbon dots-based nanocomposite: An excellent photocatalyst under sunlight irradiation. International Journal of Biological Macromolecules 2020; 164: 3676-3686. https://doi.org/10.1016/j.ijbiomac.2020.08.230

[22] Guo Y, Zhao W. Hydrothermal synthesis of highly fluorescent nitrogen-doped carbon quantum dots with good biocompatibility and the application for sensing ellagic acid. Spectrochimica Acta - Part A: Molecular and Biomolecular Spectroscopy 2020; 240: 118580. https://doi.org/10.1016/j.saa.2020.118580

[23] Hazarika D, Karak N. Photocatalytic degradation of organic contaminants under solar light using carbon dot/titanium dioxide nanohybrid, obtained through a facile approach. Applied Surface Science 2016; 376: 276–285. https://doi.org/10.1016/j.apsusc.2016.03.165

[24] Qiu Y, Wang F, Ma X, Yin F, Li D et al. Carbon quantum dots derived from cassava stems via acid/alkali-assisted hydrothermal carbonization: formation, mechanism and application in drug release. Industrial Crops and Products 2023; 204: 117243. https://doi.org/10.1016/j.indcrop.2023.117243

[25] He M, Zhang J, Wang H, Kong Y, Xiao Y. et al. Material and optical properties of fluorescent carbon quantum dots fabricated from lemon juice via hydrothermal reaction. Nanoscale Research Letters 2018; 13 (175):1-7. https://doi.org/10.1186/s11671-018-2581-2587

[26] Abd AH, Ibrahim OA. Synthesis of Carbon Quantum Dot by Electro-Chemical Method and Studying Optical, Electrical, and Structural Properties. Chemıcal Methodologıes 2022; 6(11): 823–830. https://doi.org/10.22034/chemm.2022.351559.1575

[27] Naik GG, Alam MB, Pandey V, Mohapatra D, Dubey PK. et al. Multi-Functional Carbon Dots from an Ayurvedic Medicinal Plant for Cancer Cell Bioimaging Applications. Journal of Fluorescence 2020; 30:407-418. https://doi.org/10.1007/s10895-020-02515-0

[28] Jiang G, Jiang T, Zhou H, Yao J, Kong X. Preparation of N-doped carbon quantum dots for highly sensitive detection of dopamine by an electrochemical method. RSC Advances 2015; 5: 9064–9068. https://doi.org/10.1039/c4ra16773b

[29] Chauhan P, Dogra S, Chaudhary S, Kumar R. Usage of coconut coir for sustainable production of high-valued carbon dots with discriminatory sensing aptitude toward metal ions. Materials Today Chemistry 2020; 16:100247. https://doi.org/10.1016/j.mtchem.2020.100247

[30] D'souza SL, Chettiar SS, Koduru JR, Kailasa SK. Synthesis of fluorescent carbon dots using Daucus carota subsp. sativus roots for mitomycin drug delivery. Optik 2018; 158:893-900. https://doi.org/10.1016/j.ijleo.2017.12.200

[31] Wang L, Zuo N, Sun M, Ma Y, Mominou N, et al. Deep desulfurization and denitrogenation of diesel fuel over Ir/Pr-N-CQDs-TiO_2 under ultraviolet radiation. Separation and Purification Technology 2021; 272:118861. https://doi.org/10.1016/j.seppur.2021.118861

[32] Huang C, Peng B. Photocatalytic degradation of patulin in apple juice based on nitrogen-doped chitosan-TiO_2 nanocomposite prepared by a new approach. LWT 2021; 140: 110726. https://doi.org/https://doi.org/10.1016/j.lwt.2020.110726

[33] Karthikeyan KT, Nithya A, Jothivenkatachalam K. Photocatalytic and antimicrobial activities of chitosan-TiO_2 nanocomposite. International Journal of Biological Macromolecules 2017; 104: 1762–1773. https://doi.org/10.1016/j.ijbiomac.2017.03.121

[34] Joni IM, Nulhakim L, Panatarani C. Characteristics of TiO_2 Particles Prepared by Simple Solution Method Using $TiCl_3$ Precursor. Journal of Physics: Conference Series 2018; 1080: 012042. https://doi :10.1088/1742-6596/1080/1/012042

[35] Teng F, Zhang G, Wang Y, Gao C, Chen L. et al. The role of carbon in the photocatalytic reaction of carbon/TiO_2 photocatalysts. Applied Surface Science 2014; 320:703–709. https://doi.org/10.1016/j.apsusc.2014.09.153

[36] Liu YT, Chen X, Yu J. and Ding B. Carbon-nanoplated CoS@TiO_2 nanofibrous membrane: An Interface-Engineered heterojunction for high-efficiency electrocatalytic nitrogen reduction. Angewandte Chemie 2019; 58,18903–18907. https://doi.org/10.1002/anie.201912733

[36] Xie R, Song Y, Wang F, Li J, Zhang X et al. Detection and elimination of tetracycline: Constructing multi-mode carbon dots for ultra-sensitive visual assay and CDs/TiO_2 for photocatalytic degradation. Applied Surface Science 2024; 648: 158990. https://doi.org/10.1016/J.APSUSC.2023.158990

[37] Yashwanth HJ, Rondiya SR, Eya HI, Dzade NZ, Phase DM et al. Synergy between nitrogen, phosphorus co-doped carbon quantum dots and ZnO nanorods for enhanced hydrogen production. Journal of Alloys and Compounds 2023; 937:168397. https://doi.org/10.1016/j.jallcom.2022.168397

[38] Sargin I, Yanalak G, Arslan G, Patir IH. Green synthesized carbon quantum dots as TiO_2 sensitizers for photocatalytic hydrogen evolution. International Journal of Hydrogen Energy 2019; 44(39): 21781−21789. https://doi.org/10.1016/j.ijhydene.2019.06.168

[39] Martins NCT, Ângelo J, Girão AV, Trindade T, Andrade L et al. N-doped carbon quantum dots/TiO_2 composite with improved photocatalytic activity. Applied Catalysis B: Environmental 2016; 193: 67–74. https://doi.org/10.1016/j.apcatb.2016.04.016

[40] Gao X, Ren PG, Wang J, Ren F, Dai Z et al. Fabrication of visible-light responsive TiO_2@C photocatalyst with an ultra-thin carbon layer to efficiently degrade organic pollutants. Applied Surface Science 2020; 532: 147482. https://doi.org/10.1016/j.apsusc.2020.147482

[41] Shafique M, Mahr MS, Yaseen M, Bhatti HN. CQD/TiO_2 nanocomposite photocatalyst for efficient visible light-driven purification of wastewater containing methyl orange dye. Materials Chemistry and Physics 2022; 278: 125583. https://doi.org/10.1016/j.matchemphys.2021.125583

[42] Li B, Zhang Y, Yang Y, Qiu W, Wang X et al. Synthesis, characterization, and antibacterial activity of chitosan/TiO_2 nanocomposite against Xanthomonas oryzae pv. oryzae, Carbohydrate Polymers 2016;152:825–831. https://doi.org/10.1016/j.carbpol.2016.07.070.

[43] Hao X, Sun W, Qin A, Li J et al. Carbon quantum dots induced one-dimensional ordered growth of single crystal TiO_2 nanowires while boosting photoelectrochemistry properties. Journal of Alloys and Compounds 2023; 947: 169549. https://doi.org/10.1016/j.jallcom.2023.169549

[44] Li M, Wang M, Zhu L, Li Y, Yan Z et al. Facile microwave assisted synthesis of N-rich carbon quantum dots/dual-phase TiO_2 heterostructured nanocomposites with high activity in CO_2 photoreduction. Applied Catalysis B: Environmental 2018; 231:269-276. https://doi.org/10.1016/j.apcatb.2018.03.027

[45] Jin Y, Tang W, Wang J, Ren F, Chen Z et al. Construction of biomass derived carbon quantum dots modified TiO_2 photocatalysts with superior photocatalytic activity for methylene blue degradation. Journal of Alloys and Compounds 2023; 932:167627. https://doi.org/10.1016/j.jallcom.2022.167627

[46] Tong S, Zhou J, Ding L, Zhou C, Liu Y et al. Preparation of carbon quantum dots/TiO_2 composite and application for enhanced photodegradation of rhodamine B. Colloids and

Surfaces A: Physicochemical and Engineering Aspects 2022; 648:129342. https://doi.org/10.1016/j.colsurfa.2022.129342

[47] Rosen MJ. Surfactants and Interfacial Phenomena. Surfactants and Interfacial Phenomena 2004; https://doi.org/10.1002/0471670561

[48] Wei TY, Kuo CY, Hsu YJ, Lu SY, Chang YC. Tin oxide nanocrystals embedded in silica aerogel: Photoluminescence and photocatalysis. Microporous and Mesoporous Materials 2008; 112(1-3):580-588. https://doi.org/10.1016/j.micromeso.2007.10.040

[49] Idris MB, Sakthivel G, Devaraj S. Textural properties dependent supercapacitive performances of mesoporous graphitic carbon nitride. Materials Today Energy 2018; (10):325-335. https://doi.org/10.1016/j.mtener.2018.10.012

[50] Yu Y, Zhou L, Tang J, Wu P, Feng L et al. Effective Removal of Co(II) and Sr(II) from Radiocative Wastes Using Covalent Triazine Frameworks: Kinetics and Isotherm Studies. Separation and. Purification Technology. 2021;277: 119633 https://doi.org/10.1016/j.micromeso.2019

[51] Sharma S, Kumar S, Arumugam SM, Elumalai S. Promising photocatalytic degradation of lignin over carbon quantum dots decorated TiO_2 nanocomposite in aqueous condition. Applied Catalysis A: General 2020; 602:117730. https://doi.org/10.1016/j.apcata.2020.117730

[52] Kılıç D, Sevim M, Eroğlu Z, Metin Ö, Karaca S. Strontium oxide modified mesoporous graphitic carbon nitride/titanium dioxide nanocomposites (SrO-mpg-CN/TiO_2) as efficient heterojunction photocatalysts for the degradation of tetracycline in water. Advanced Powder Technology 2021; 32(8):2743-2757. https://doi.org/10.1016/j.apt.2021.05.043

[53] Hao X, Sun W, Qin A, Li J, Huang W et al. Carbon quantum dots induced one-dimensional ordered growth of single crystal TiO_2 nanowires while boosting photoelectrochemistry properties. Journal of Alloys and Compounds 2023; 947:169549. https://doi.org/10.1016/j.jallcom.2023.169549

[54] Sun X, Li HJ, Ou N, Lyu B et al. Visible-Light Driven TiO_2 Photocatalyst Coated with Graphene Quantum Dots of Tunable Nitrogen Doping. Molecules 2019;24(2):344. https://doi.org/10.3390/molecules24020344

[55] Singh H, Singh S, Bhardwaj SK, Kaur G, Khatri M et al. Development of carbon quantum dot-based lateral flow immunoassay for sensitive detection of aflatoxin M1 in milk. Food Chemistry 2022; 393:133374. https://doi.org/10.1016/j.foodchem.2022.133374

[56] Aghamali A, Khosravi M, Hamishehkar H, Modirshahla N, Behnajady MA. Preparation of novel high performance recoverable and natural sunlight-driven nanocomposite

photocatalyst of Fe_3O_4/C/TiO_2/N-CQDs. Materials Science in Semiconductor Processing 2018; 87: 142-154. https://doi.org/10.1016/j.mssp.2018.07.018

[57] Xu L, Bai X, Guo L, Yang S, Jin P et al. Facial fabrication of carbon quantum dots (CDs)-modified N-TiO_{2-x} nanocomposite for the efficient photoreduction of Cr(VI) under visible light. Chemical Engineering Journal 2019; 357:473-486. https://doi.org/10.1016/j.cej.2018.09.172

[58] Oseghe EO, Ofomaja AE. Facile microwave synthesis of pine cone derived C-doped TiO_2 for the photodegradation of tetracycline hydrochloride under visible-LED light. Journal of Environmental Management 2018; 223:860-867. https://doi.org/10.1016/j.jenvman.2018.07.003

[59] Shen T, Wang Q, Guo Z, Kuang J, Cao W. Hydrothermal synthesis of carbon quantum dots using different precursors and their combination with TiO_2 for enhanced photocatalytic activity. Ceramics International 2018; 44(10):11828-11834. https://doi.org/10.1016/j.ceramint.2018.03.271

[60] Madihi-Bidgoli S, Asadnezhad S, Yaghoot-Nezhad A, Hassani A. Azurobine degradation using Fe_2O_3@multi-walled carbon nanotube activated peroxymonosulfate (PMS) under UVA-LED irradiation: performance, mechanism and environmental application. Journal of Environmental Chemical Engineering 2021; 9(6):106660. https://doi.org/10.1016/j.jece.2021.106660

[61] Meng L, Zhao C, Wang T, Chu H, Wang CC. Efficient ciprofloxacin removal over Z-scheme ZIF-67/V-$BiOIO_3$ heterojunctions: Insight into synergistic effect between adsorption and photocatalysis. Separation and Purification Technology 2023; 313: 123511. https://doi.org/10.1016/j.seppur.2023.123511

[62] Martínez C, Vilariño S, Fernández MI, Faria J, Canle ML et al. Mechanism of degradation of ketoprofen by heterogeneous photocatalysis in aqueous solution. Applied Catalysis B: Environmental 2013; 142–143: 633-646. https://doi.org/10.1016/j.apcatb.2013.05.018

[63] Hassani A, Eghbali P, Kakavandi B, Lin KYA, Ghanbari F. Acetaminophen removal from aqueous solutions through peroxymonosulfate activation by $CoFe_2O_4$/mpg-C_3N_4 nanocomposite: Insight into the performance and degradation kinetics. Environmental Technology and Innovation 2020; 20:101127. https://doi.org/10.1016/j.eti.2020.101127

[64] Hassani A, Khataee A, Karaca S, Fathinia M. Heterogeneous photocatalytic ozonation of ciprofloxacin using synthesized titanium dioxide nanoparticles on a montmorillonite support: parametric studies, mechanistic analysis and intermediates identification. RSC Adv, Royal Society of Chemistry 2016; 6: 87569–87583. https://doi.org/10.1039/c6ra19191f

[65] Ozer M.S, Eroglu Z, Yalin A.S, Kılıç M, Rothlisberger U et al. Bismuthene as a versatile photocatalyst operating under variable conditions for the photoredox C-H bond

functionalization. Applied Catalysis B: Environmental 2022; 304:120957. https://doi.org/10.1016/j.apcatb.2021.120957

[66] Eroglu Z, Metin O. Internal Interactions within the Complex Type-II Heterojunction of a Graphitic Carbon Nitride/Black Phosphorus Hybrid Decorated with Graphene Quantum Dots: Implications for Photooxidation Performance. ACS Applied Nano Materials 2023; 6(9):7960-7974. https://doi.org/10.1021/acsanm.3c01187

[67] Xiong J, Li X, Huang J, Gao X, Chen Z et al. CN/rGO@BPQDs high-low junctions with stretching spatial charge separation ability for photocatalytic degradation and H_2O_2 production. Applied Catalysis B: Environmental 2020; 266: 118602. https://doi.org/10.1016/j.apcatb.2020.118602

[68] Eroglu Z, Ozer M.S, Metin O. Black Phosphorus Quantum Dots/Carbon Nitride-Reduced Graphene Oxide Ternary Heterojunction as a Multifunctional Metal-Free Photocatalyst for Photooxidation Reactions. ACS Sustainable Chemistry and Engineering 2023; 11(19):7560-7572. https://doi.org/10.1021/acssuschemeng.3c01055

[69] Li X, Luo Q, Han L, Deng F, Yang Y et al. Enhanced photocatalytic degradation and H_2 evolution performance of 0D/2D N-CDs/S-C_3N_4 S-scheme heterojunction constructed by π-π conjugate self-assembly. Journal of Materials Science & Technology 2022; 114:222-232. https://doi.org/10.1016/j.jmst.2021.10.030

[70] Eroglu Z, Sündü B, Metin O. Tailoring the redox ability of carbon nitride quantum dots/reduced graphene oxide-black phosphorus (CNQDs@rGOBP) ternary heterojunctions for photodegradation of organic pollutants. Materials Today Sustainability 2023; 23:100418. https://doi.org/10.1016/j.mtsust.2023.100418

[71] Xu Q, Zhang L, Cheng B, Fan J, Yu J. S-Scheme Heterojunction Photocatalyst. Chem 2020; 6 (7): 1543-1559. https://doi.org/10.1016/j.chempr.2020.06.010

[72] Li X, Kang B, Dong F, Zhang Z, Luo X et al. Enhanced photocatalytic degradation and H_2/H_2O_2 production performance of S-pCN/$WO_{2.72}$ S-scheme heterojunction with appropriate surface oxygen vacancies. Nano Energy 2021; 81: 105671. https://doi.org/10.1016/j.nanoen.2020.105671

[73] Zhang J, Liu Q, He H, Shi F, Huang G et al. Coal tar pitch as natural carbon quantum dots decorated on TiO_2 for visible light photodegradation of rhodamine B. Carbon 2019; 152: 284-294. https://doi.org/10.1016/j.carbon.2019.06.034

[74] Zhang N, Ning X, Chen J, Xue J, Lu G et al. Photocatalytic degradation of tetracycline based on the highly reactive interface between graphene nanopore and TiO_2 nanoparticles. Microporous and Mesoporous Materials 2022; 338: 111958. https://doi.org/10.1016/j.micromeso.2022.111958

[75] Mahmood A, Shi G, Wang Z, Rao Z, Xiao W et al. Carbon quantum dots-TiO_2 nanocomposite as an efficient photocatalyst for the photodegradation of aromatic ring-

containing mixed VOCs: An experimental and DFT studies of adsorption and electronic structure of the interface. Journal of Hazardous Materials 2021; 401: 123402. https://doi.org/10.1016/j.jhazmat.2020.123402

[76] Rajender G, Kumar J, Giri P.K. Interfacial charge transfer in oxygen deficient TiO_2-graphene quantum dot hybrid and its influence on the enhanced visible light photocatalysis. Applied Catalysis B: Environmental 2018; 224: 960-972. https://doi.org/10.1016/j.apcatb.2017.11.042

FIGURES

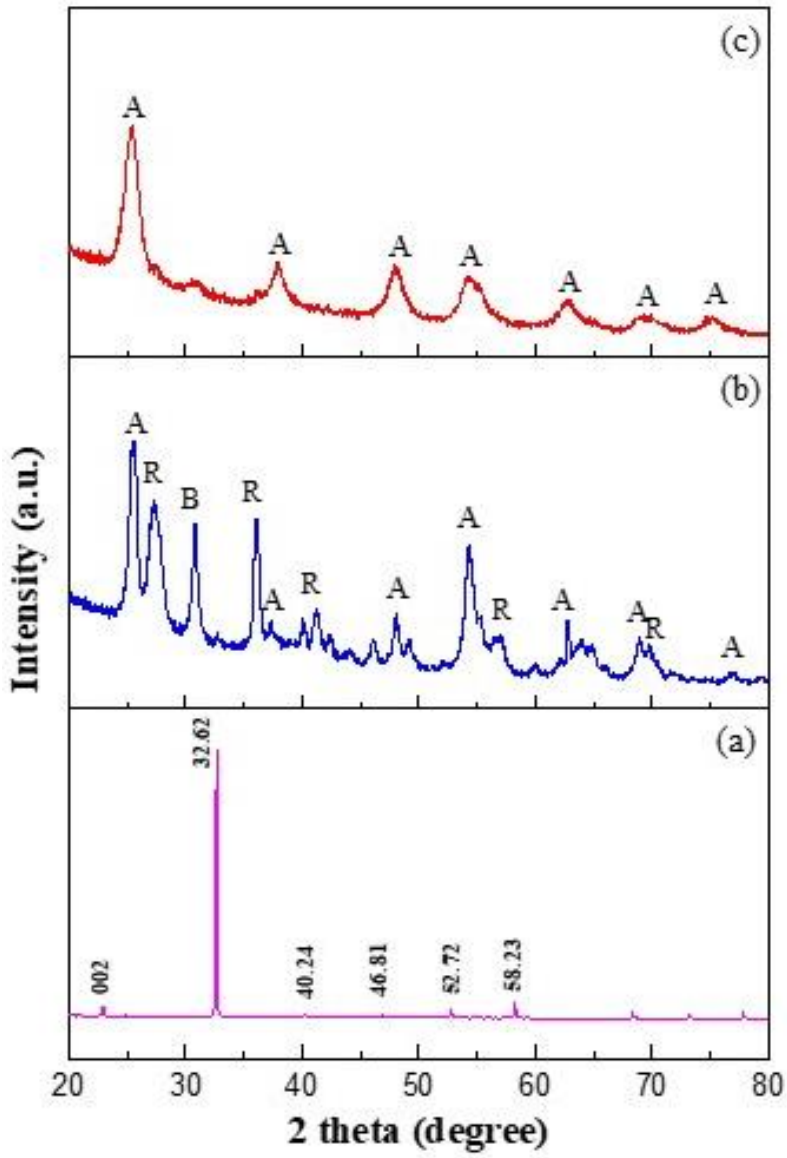

Figure 1. XRD patterns of **a)** *N*-CQDs **b)** TiO_2, and **c)** *N*-CQDs/TiO_2 nanocomposite.

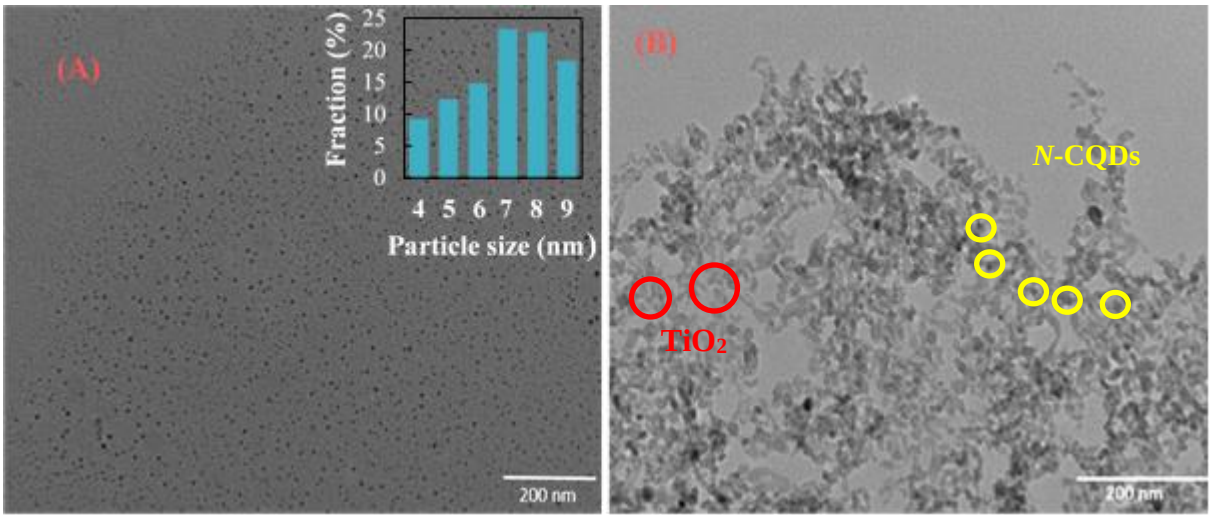

Figure 2. Representative TEM images of (A) *N*-CQDs and (B) *N*-CQDs/TiO_2 heterojunction photocatalyst

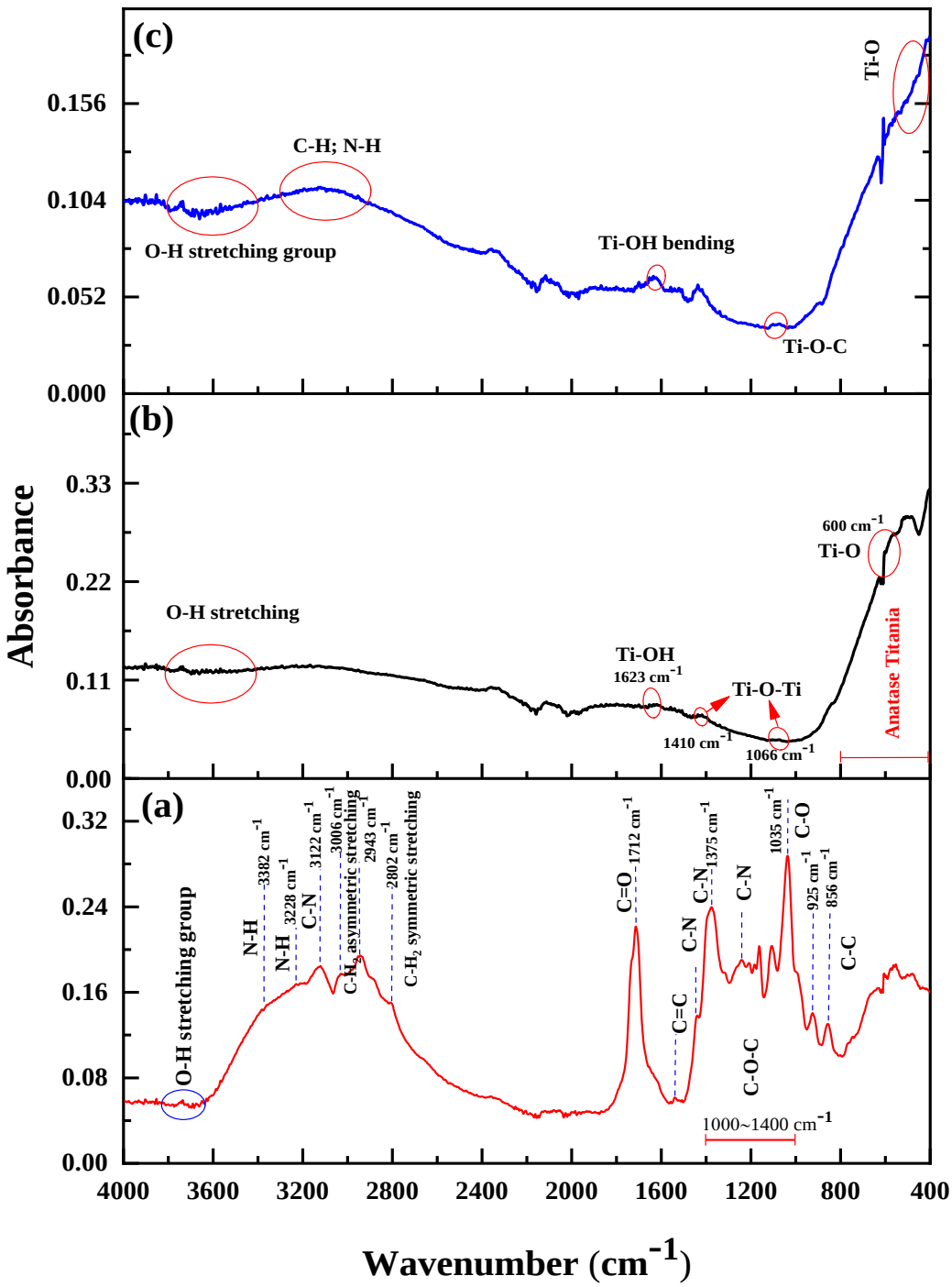

Figure 3. FTIR spectra of as-prepared (a) *N*-CQDs, and (b) TiO_2, and (c) *N*-CQDs/TiO_2 nanocomposite, respectively.

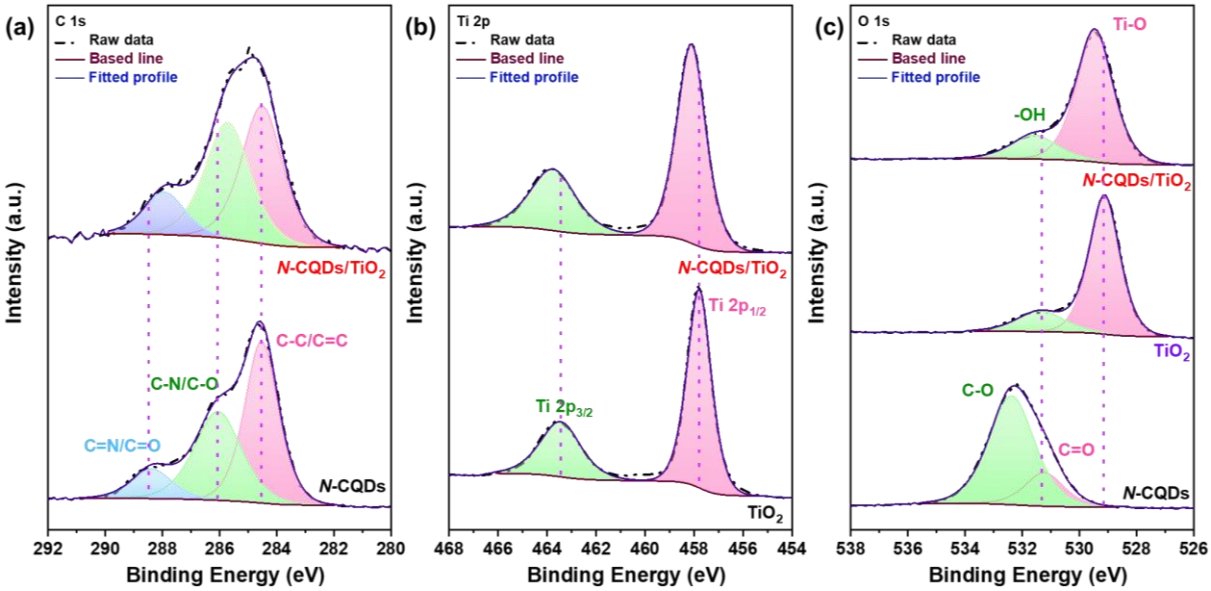

Figure 4. (a) High-resolution C1s XPS spectra of *N*-CQDs, and *N*-CQDs/TiO_2 nanocomposites. (b) high-resolution Ti 2p XPS spectra of TiO_2, and *N*-CQDs/TiO_2 nanocomposites. (c) high-resolution O 1s XPS spectra of *N*-CQDs, TiO_2, and *N*-CQDs/TiO_2 nanocomposites.

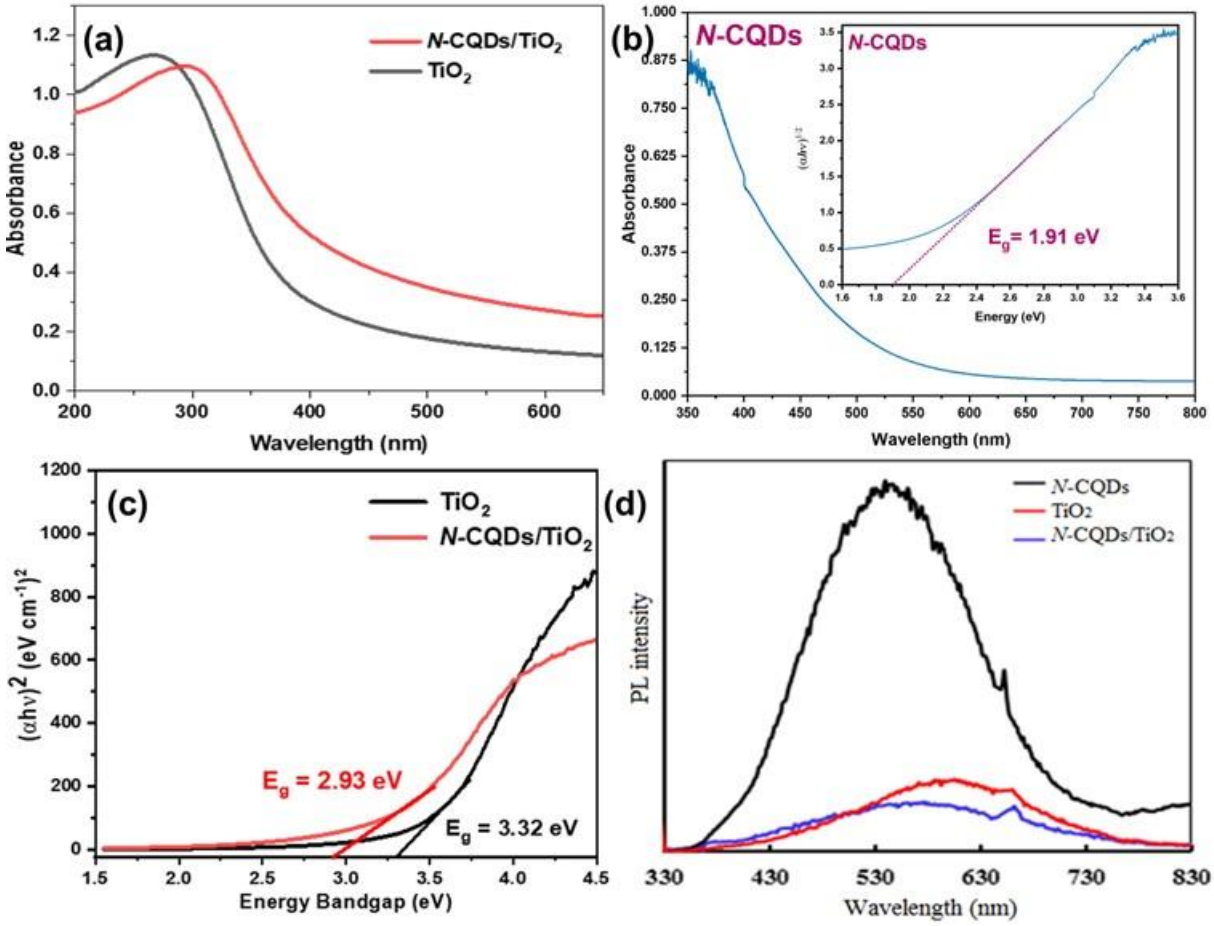

Figure 5. UV–Vis DRS spectra of TiO_2 and *N*-CQDs/TiO_2 nanocomposites (a), *N*-CQDs (b), the inset of (b) shows the band gap energy (Eg) of the as-prepared *N*-CQDs, Tauc plots of TiO_2 and *N*-CQDs/TiO_2 nanocomposites (c), PL emission spectra under excitation wavelength of 325 nm of as-prepared *N*-CQDs, TiO_2 and *N*-CQDs/TiO_2 nanocomposites (d).

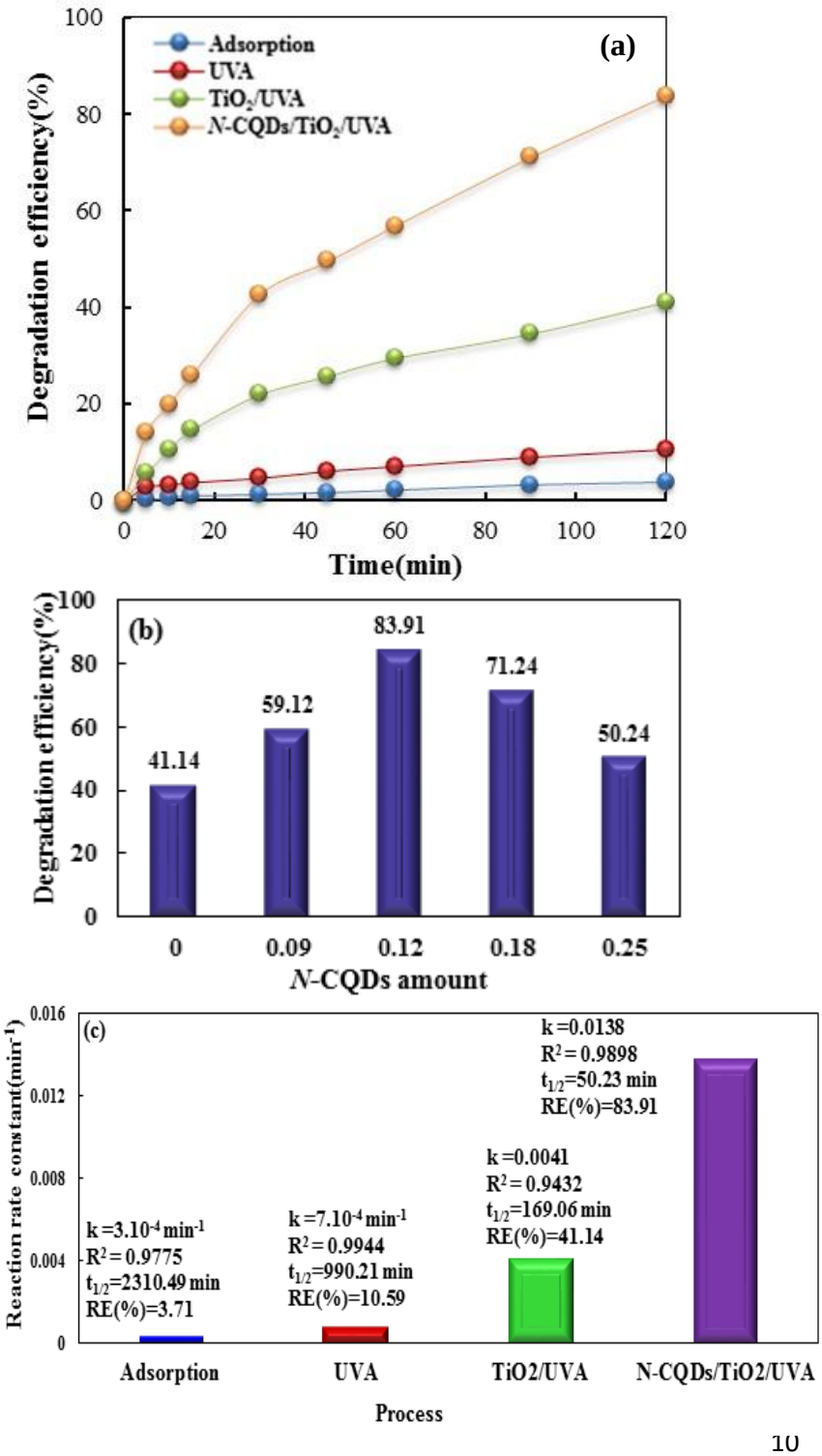

Figure 6. a) The effect of different processes on the removal efficiency of CIP, b) The impact of *N*-CQDs amount on the CIP degradation using *N*-CQDs/TiO_2 nanophotocatalyst, **c**) Degradation efficiencies and kinetic parameters for CIP degradation via different processes. Experimental conditions: $[Catalyst]_0$ = 0.4 g/L, $[CIP]_0$ = 10 mg /L, and pH =5

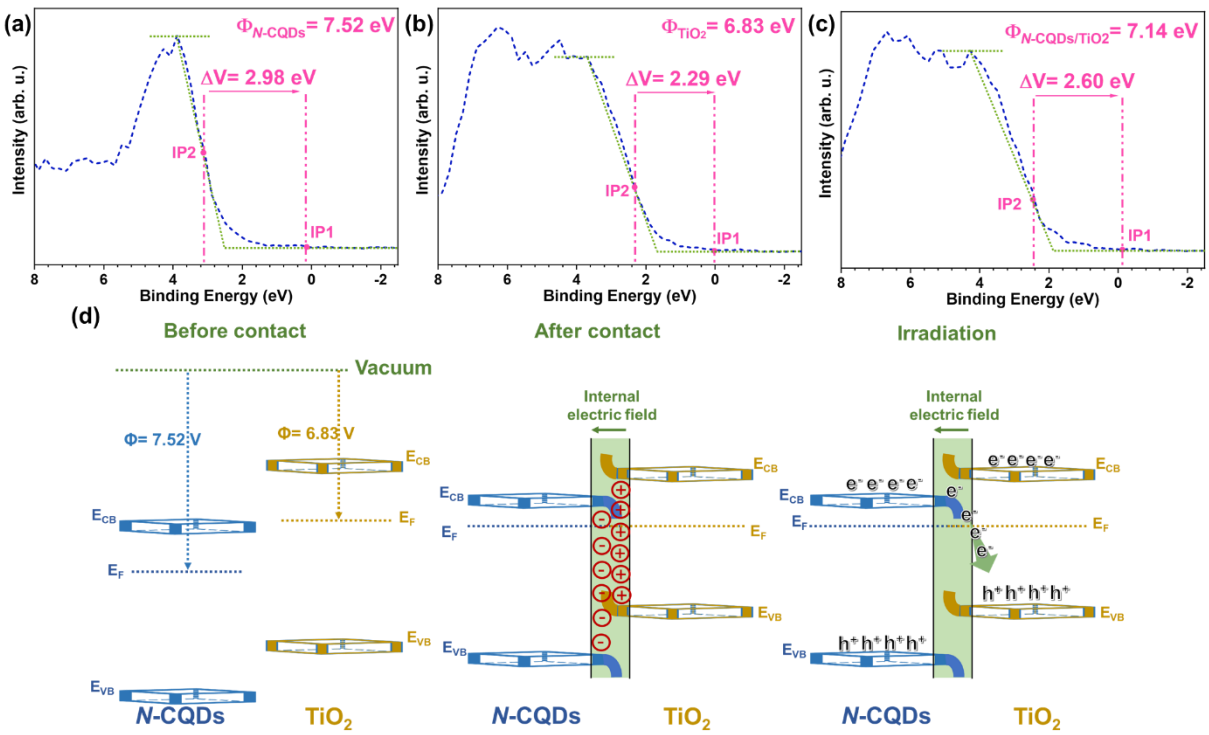

Figure 7. The work functions of **a)** *N*-CQDs **b)** TiO_2 **c)** *N*-CQDs/TiO_2 and **d)** IEF between semiconductors, before, after contact and under irradiation, respectively and the resulted bending of band edges for *N*-CQDs, and TiO_2.

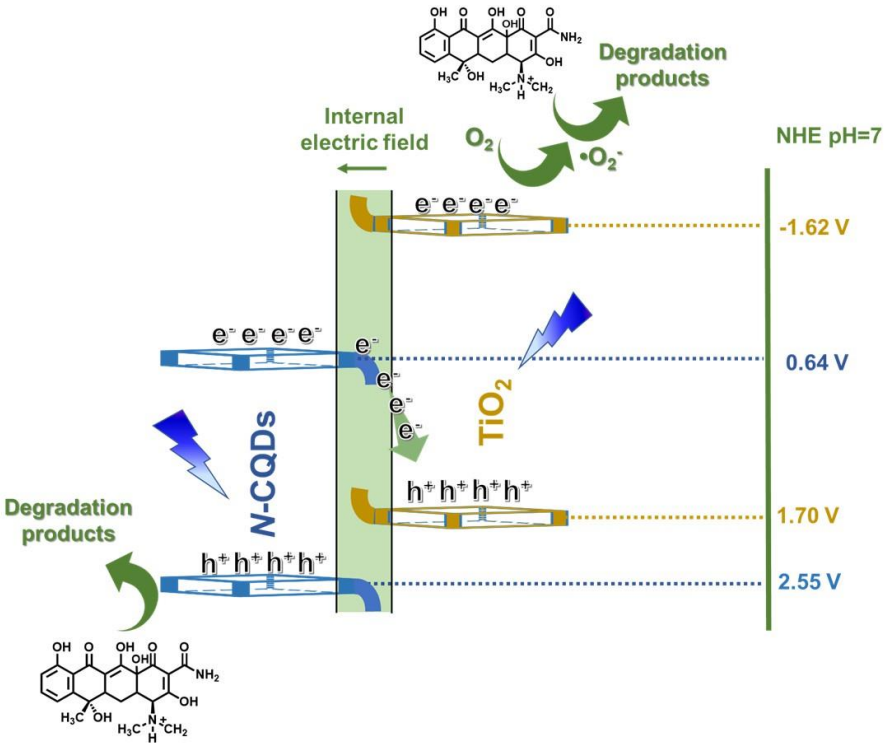

Figure 8. A schematic illustration of the photocatalytic mechanism for the photodegradation of CIP in the presence of *N*-CQDs/TiO_2 nanocomposite.

Exploring the efficiency of nitrogenated carbon quantum dots/TiO_2 S-scheme heterojunction in photodegradation ciprofloxacin in aqueous environments

Yılmaz ATEŞ[a], Zafer EROĞLU[b], Özkan AÇIŞLI[a], Önder METIN[b,c], Semra KARACA[a,*]

[a]Department of Chemistry, Faculty of Science, Atatürk University, 25240 Erzurum, Turkey

[b]Department of Chemistry, College of Sciences, Koç University, 34450 Sarıyer, Istanbul, Turkey

[c] Koç University Surface Science and Technology Center (KUYTAM), 34450 Sarıyer, Istanbul, Turkey

*Correspondence: skaraca@atauni.edu.tr

ORCIDs:

Yılmaz Ateş: https://orcid.org/0000-0003-0965-6279

Zafer Eroğlu: https://orcid.org/0000-0002-0601-2526

Özkan Açışlı: https://orcid.org/0000-0002-4465-0916

Önder Metin: https://orcid.org/0000-0003-1622-4992

Semra Karaca: https://orcid.org/0000-0001-8627-5803

Materials

Chitosan sample with 75% deacetylation degree (DD) of ca.was bought from Sigma-Aldrich Co. (USA). Glycerol ($C_3H_8O_3$, 99.5) from Tekkim, acetic acid (CH_3COOH, ≥99.5%) and Urea (H_2N-CO-NH_2, 99%) from Merck, titanium(IV) ethoxide (TiO_2, >99%), ethanol (C_2H_5OH, 99%), and ciprofloxacin (CIP, 96%) from Sigma Aldrich, hydrochloric acid (HCl, 37%) from Riedel-De-Haën were purchased. Millipore Milli-Q deionized water with properties of 20 µs/cm, approximate ionic concentration Type 3 water of 10 mg/L and 25 °C was used from Millipore Direct Q 8uv (Millipore, U.S.A.) in all experiments. The characteristics and chemical structure of Ciprofloxacin (CIP) are illustrated in Table S1.

Table S1 Structure and characterization of Ciprofloxacin (CIP)

Chemical structure	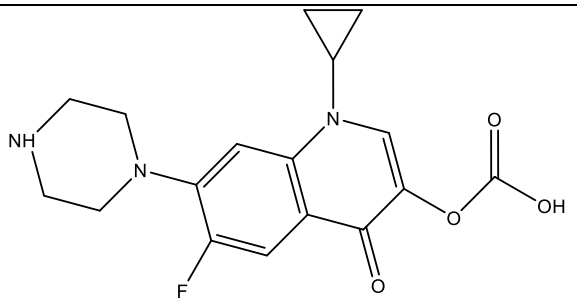
Molecular formula	$C_{17}H_{18}FN_3O_3$
Mw g/mol)	331.346
λmax (nm)	276
Solubilitiy in water (mg/mL)	30
Therapeutic group	Antibiotic

2. Instrumentation

Scanning electron microscopy (SEM, Zeiss Sigma 300,Germany) and transmission electron microscopy equipped with EXA- LENS (TEM, Hitachi HT7700 TEM, Japan) with an actuated at 120 kV were used to characterize the morphologies of *N*-CQDs, TiO_2 and *N*-CQDs/TiO_2 samples, and the energy-dispersive X-ray spectroscopy (EDX, Zeiss,

Germany) was used for elemental analysis. The powder X-ray diffraction (XRD) patterns have been recorded on a Rigaku Advanced Powder X-ray Diffraction meter operating at 30 kV and 30 mA with CuKα radiation in the 2θ of 20-80° range (0.154051 nm) to examine the crystal structure of the synthesized samples. The chemical composition and the oxidation state of the elements in the as-prepared catalyst samples was tested by X-ray Photo Electron Spectroscopy (XPS, Thermo K-Alpha). To calculate the binding energy adjustment, the C1s peak (284.5 eV) was used as a reference peak. The indium tin oxide (ITO) surface was coated with *N*-CQDs via the drop-casting method. Fourier transform infrared spectra (FT-IR) were obtained by a Tensor 27 Bruker spectrometer (Germany) employing KBr pellets with a scanning range from 4000 to 400 cm^{-1}. N_2 nitrogen adsorption-desorption isotherms at 77K were performed on a Micromeritics 3 Flex instrument (Micrometrics Instruments, USA). The surface areas of as-prepared samples were computed by the Brunauer–Emmett–Teller (BET) method, and the pore size distributions were determined by the Barrett–Joyner–Halenda (BJH) method from the desorption branch of the isotherms. The removal efficiency of CIP measurements was performed with Varian Cary 100 UV-VIS Spectrophotometer device (Varian Cary 100, Australia). Photoluminescence (PL) spectra of as-prepared samples were measured using a Shimadzu RF-5301PC spectrofluorophotometer by excitation at 325 nm with a 150 W Xe lamp. The zero-charge point (zpc) of *N*-CQDs/TiO_2 nanocomposite was found by Malvern Zetasizer Nano ZSP (Malvern Inst.Ltd., UK). A Shimadzu UV-2550 spectrophotometer (Japan) was used to record UV–vis DRS of the synthesized samples.

3. Synthesis of TiO_2

0.3 g of urea and 1.6 mL of titanium(IV) ethoxide were drop wisely added to the concentrated HCl solution mixed with 25 mL of water, and after mixing again, the

mixture was transferred to the Teflon lined stainless reactor and kept at 150 °C for 6 hours. The reactor content, brought to ambient temperature, were centrifuged at 9000 rpm for 10 min. The solid part was separated and dried at 80 °C for 7-8 h. This solid product was calcined in a muffle furnace at 300°C for 2 hours.

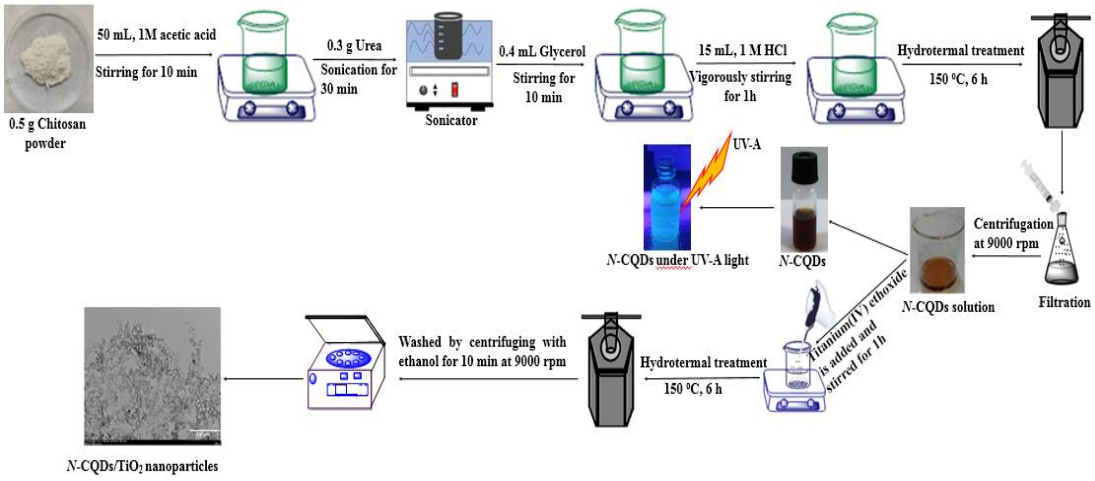

Figure S1. Synthesis flowchart of *N*-CQDs/TiO_2 nanocomposites.

Experimental device and the procedure

The experimental device for photocatalytic degradation of ciprofloxacin was conducted in a magnetically stirred quartz cylindrical reactor with a working volume of 500 mL (reactor vessel dimensions 50.0 mm × 250.0 mm, Çalışkan Cam, Turkey). Magnetic stirring was used to achieve effective interaction between the catalysts and the organic contaminate. The outer surface of the reactor was completely covered with aluminum foil to obtain maximum efficiency from the UV source. 16 W UV-A (Sylvania, Japan) was used as the UV irradiation source. Batch studies were carried out with the constant CIP solution of 500 mL to determine the effects of various processing variables, catalyst dosage (0.05–0.60 g/L), initial CIP concentration (5–25 mg/L) and pH (2–10), on the degradation efficiency of CIP. The pH value was adjusted by adding 0.1 M HCl or NaOH solution using a pH meter (Mettler Toledo, China). The suspension was then agitated in dark for 20 min to reach the equilibrium. Afterward, the UV-A lamp was placed into the

reactor and turned on. In addition, adsorption experiments conducted without UV irradiation were also performed in covered beakers to ensure similar processing conditions with the photo-catalytic experiments. At the predetermined time intervals, approximately 3 mL solution was taken and then centrifuged at 5000 rpm for 4 min. In order to stop the photocatalytic reactions in the filtrate, 0.5 mL methanol was added to the solution. The remaining CIP concentration was finally measured using a Varian Cary 100 UV–vis spectrophotometer at the maximum wavelength of 276 nm. The degradation efficiency (%) of CIP was calculated from the below equation:

$$Degradation\ efficiency = \left[\frac{A_0 - A_t}{A_0}\right] x100$$

in which A_0 and A_t exemplify the CIP absorbance values for the initial and after t period (min).

5.Catalyst characterization

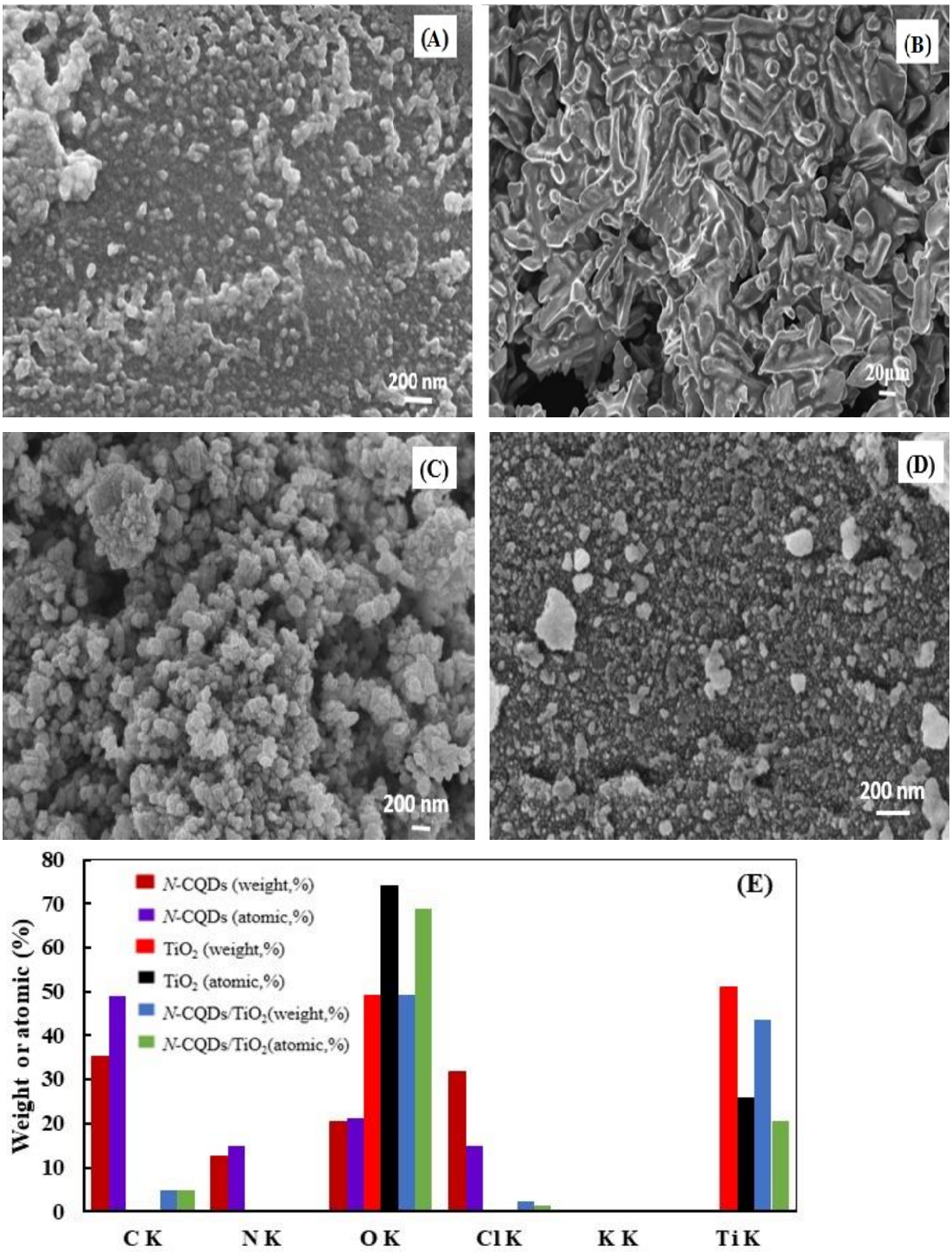

Figure S2. SEM images of *N*-CQDs with different magnification (A, B), bare TiO_2 (C) *N*-CQDs/TiO_2 nanocomposite (D), and their EDX spectrum (E)

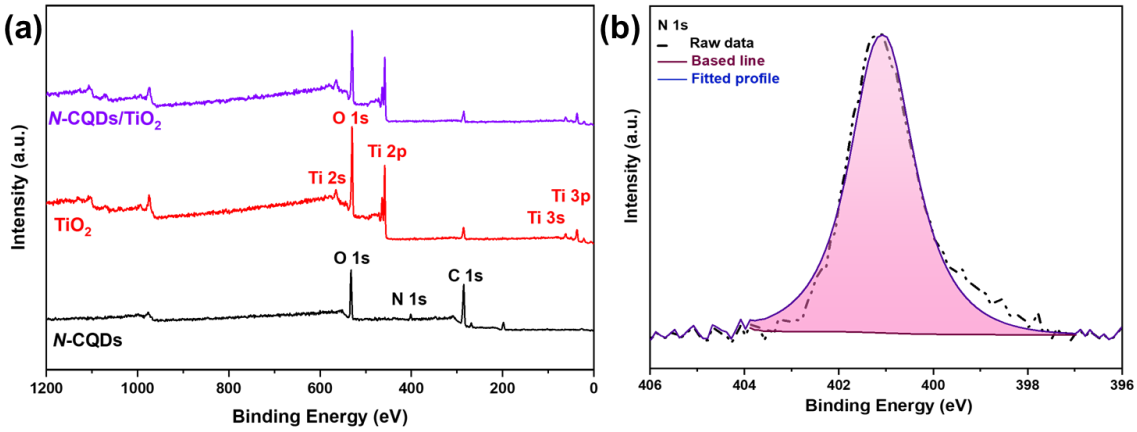

Figure S3. (a) XPS survey spectra of as-prepared *N*-CQDs, TiO_2, and *N*-CQDs/TiO_2 nanocomposite and (b) high resolution XPS N 1s spectra for *N*-CQDs

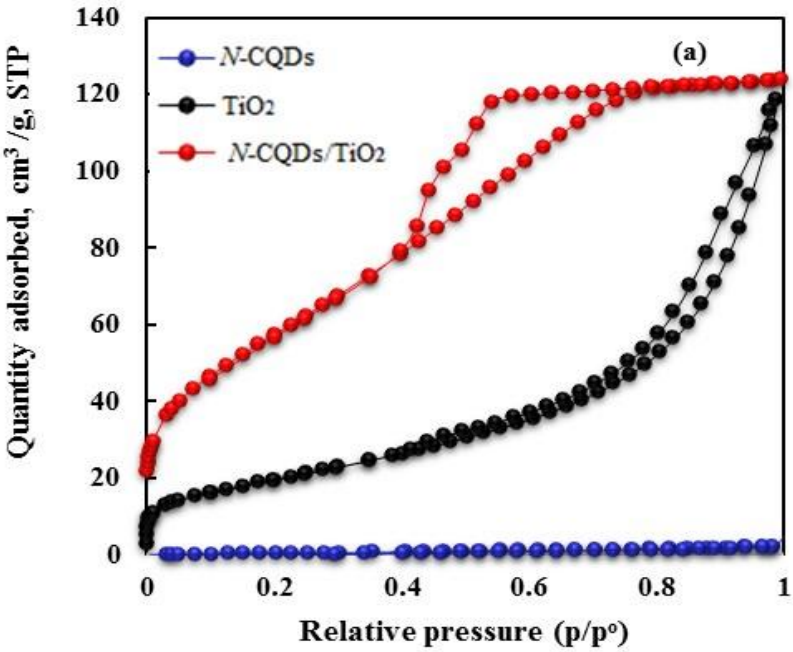

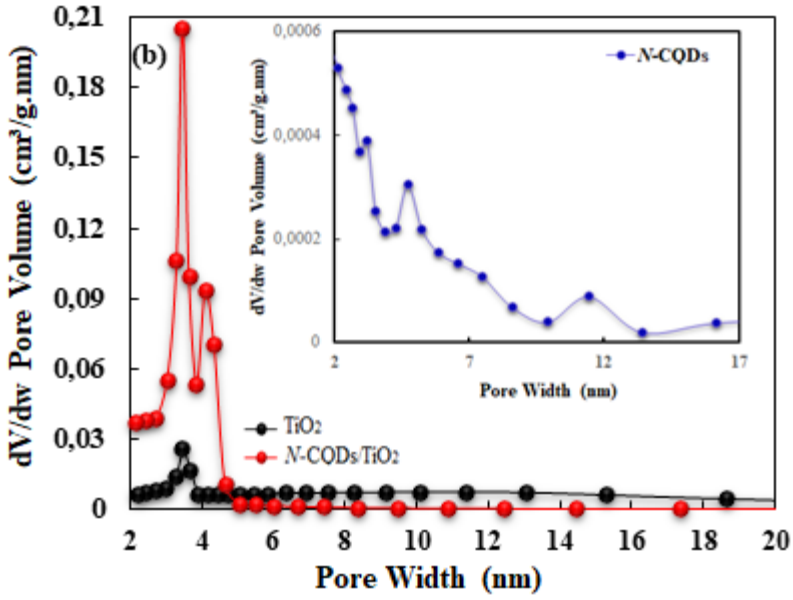

Figure S4. (a) N_2 adsorption-desorption isotherms for *N*-CQDs, TiO_2, and *N*-CQDs/TiO_2 nanocomposites, **(b)** BJH pore size distribution of the corresponding materials.

6.Photocatalytic CIP Degradation

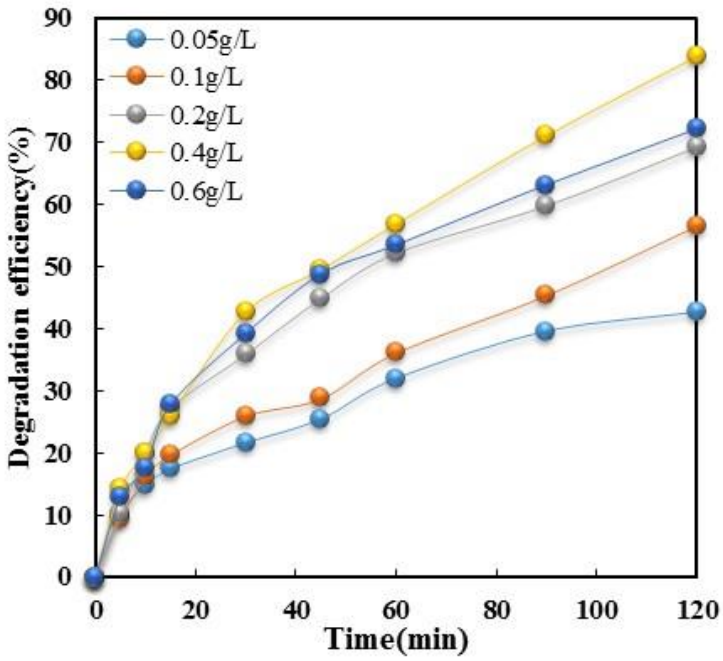

Figure S5. Photocatalytic degradation of CIP at different *N*-CQDs/TiO_2 loading. Experimental conditions: $[CIP]_0$= 10 mg /L, and pH=5.

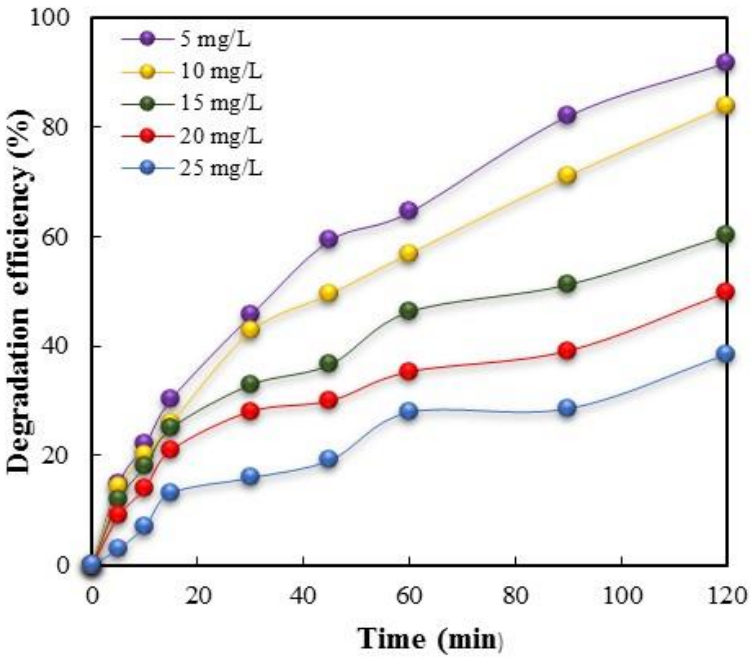

Figure S6. The variation of CIP degradation with initial CIP concentration and reaction time. Experimental conditions: [*N*-CQDs/TiO_2]$_0$= 0.4 g/L, and pH=5.

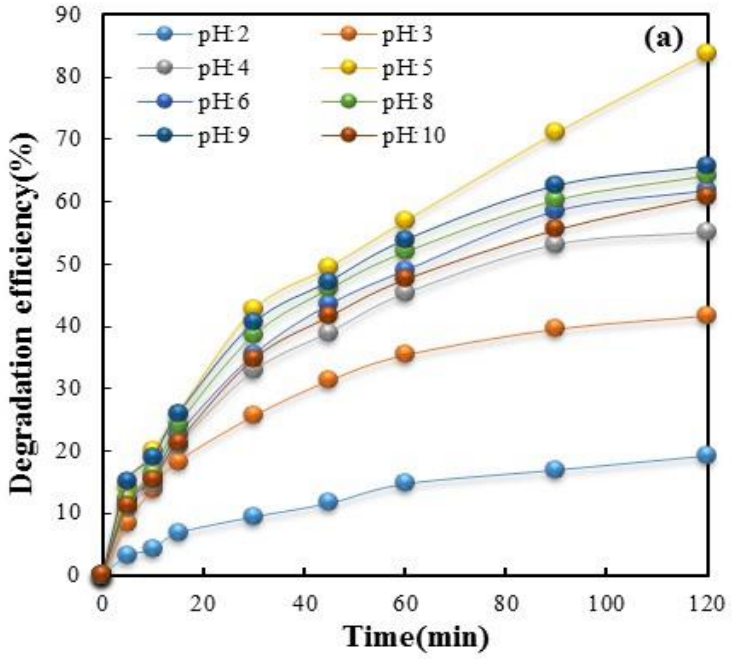

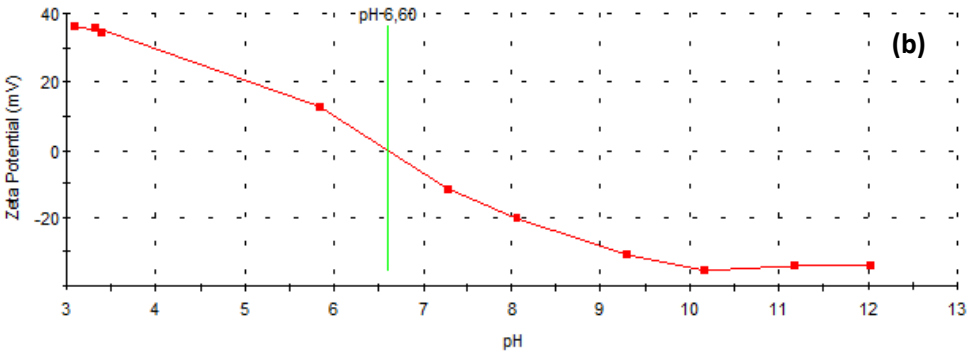

Figure S7. (a) Impact of initial solution pH. Experimental conditions : $[CIP]_0$ = 10 mg/L, and $[Catalyst]_0$ = 0.4 g/L **(b)** Zero point of charge (pH_{zpc}) for *N*-CQDs/TiO_2

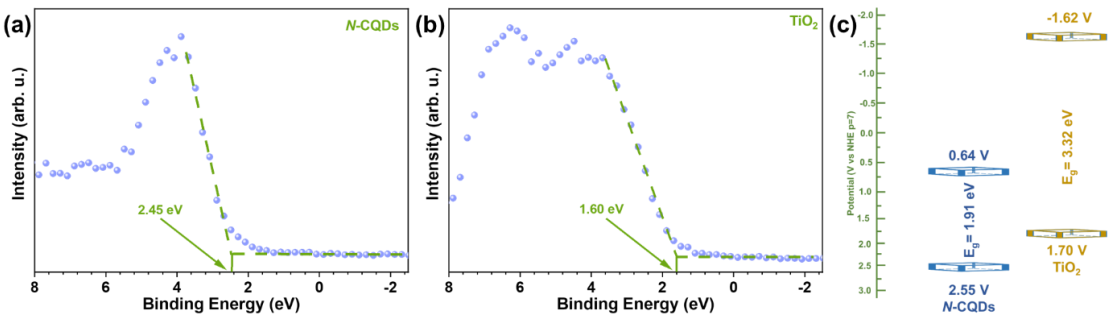

Figure S8 VB-XPS analyses of (a) *N*-CQDs (b) TiO_2 (c) band alignments of *N*-CQDs, and TiO_2.

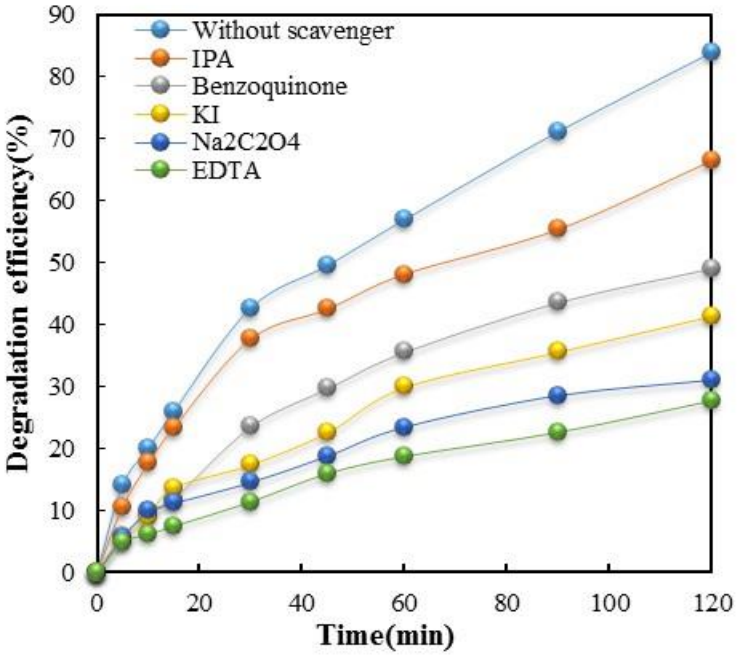

Figure S9. Impact of scavengers. Conditions: $[CIP]_0$ = 10 mg/L, and $[Catalyst]_0$ = 0.4 g/L, $[Scavenger]_0$ = 10 mg/L, and pH = 5.

Table S2. Textural characteristics of the as-synthesized materials of TiO_2, *N*-CQDs, *N*-CQDs/TiO_2

Parameter	**TiO_2**	***N*-CQDs**	*N*-CQDs/**TiO_2**
BET surface area (m^2/g)	71.798	1.091	213.792
BJH cumulative surface area (m^2/g)	78.025	2.367	252.690
Total pore volume (cm^3/g)[(a)]	0.186	0.003	0.203
BJH Desorption average pore width (nm)[b]	9.524	5.171	3.210

[a] Obtained by the BJH method.
[b]Computed by the BJH (desorption) method using N_2 adsorption isotherm.

Table S3. Comparison of the CIP degradation efficiencies with reported different photocatalysts

Photocatalysts	Catalyst loading (g/L)	CIP concentration (mg/L)	Reaction time (min)	Degradation efficiency (%)	References
MIL100(Fe)@DPANI@CelF	0.25	32	180	82.78	[1]
ZnO	0.02	5	60	48	[2]
NiS/MoS_2/C_3N_4	1.00	10	120	71.3	[3]
BiOCl	0.25	10	240	74	[4]
Sepiolite/g-C_3N_4/Pd	0.40	10	60	64	[5]
Co-BiOCl/CQDs	0.50	20	100	79.6	[6]
CQDs/$PbBiO_2Cl$	0.30	10	75	78.9	[7]
N-CQDs/TiO_2 nanocomposite	0.40	10	120	83.91	This work

References

[1] Hou X, Sun L, Hu Y, An X, Qian X. De-doped polyaniline as a mediating layer promoting in-situ growth of metal–Organic frameworks on cellulose fiber and enhancing adsorptive-photocatalytic removal of ciprofloxacin. Polymers, 2021; 13(19):3298. https://doi.org/10.3390/polym13193298

[2] El-Kemary M, El-Shamy H, and El-Mehasseb I. Photocatalytic degradation of ciprofloxacin drug in water using ZnO nanoparticles. Journal of Luminescence, 2010; 130(12) : 2327-2331. https://doi.org/10.1016/j.jlumin.2010.07.013

[3] Lu X, Wang Y, Zhang X, Xu G, Wang D et al. NiS and MoS_2 nanosheet co-modified graphitic C_3N_4 ternary heterostructure for high efficient visible light photodegradation

of antibiotic. Journal of Hazardous Materials, 2018; 341:10-19. https://doi.org/10.1016/j.jhazmat.2017.07.004

[4] Senasu T, Narenuch T, Wannakam K, Chankhanittha T, Nanan S. Solvothermally grown BiOCl catalyst for photodegradation of cationic dye and fluoroquinolone-based antibiotics. Journal of Materials Science: Materials in Electronics, 2020; 31:9685-9694. https://doi.org/10.1007/s10854-020-03514-4

[5] Chuaicham C, Pawar RR, Karthikeyan S, Ohtani B, Sasaki K. Fabrication and characterization of ternary sepiolite/g-C_3N_4/Pd composites for improvement of photocatalytic degradation of ciprofloxacin under visible light irradiation. Journal of Colloid and Interface Science, 2020; 577: 397–405. https://doi.org/https://doi.org/10.1016/j.jcis.2020.05.064

[6] Li W, Huang J, Fu X, Xu J, Yu X et al. CQDs modified Co-BiOCl nanosheets with improved effective light absorption and charge separation for photocatalytic CIP degradation and NOX removal. Surfaces and Interfaces, 2021; 27: 101541. https://doi.org/10.1016/j.surfin.2021.101541

[7] Sheng Y, Yi D, Qingsong H, Ting W, Ming L et al. CQDs modified $PbBiO_2Cl$ nanosheets with improved molecular oxygen activation ability for photodegradation of organic contaminants. Journal of Photochemistry and Photobiology A: Chemistry, 2019; 382: 111921. https://doi.org/10.1016/j.jphotochem.2019.111921